NASS - Effect of rotation

Dehaeze Thomas

March 21, 2024

Contents

An important aspect of the Nano Active Stabilization System (NASS) is that the nano-hexapod is continuously rotating around a vertical axis while the external metrology is not. Such rotation induces gyroscopic effects that may impact the system dynamics and obtained performances.

In this report, this rotating aspect of the NASS is studied. It is structured in several sections:

- Section 1: a simple model of a rotating suspended platform that will be used throughout this study is presented. The effect of the rotation velocity on the system dynamics is shown.
- Section 2: Integral Force Feedback (IFF) is applied to the rotating platform, and it is shown that the unconditional stability of IFF is lost due to Gyroscopic effects induced by the rotation.
- Section 3: A first modification of the IFF control law is proposed such that damping can be added to the suspension modes in a robust way. This modification consists of adding an high pass filter to the IFF controller. Optimal high pass filter cut-off frequency is computed.
- Section 4: A second modification is proposed to regain the unconditional stability of IFF. This modification consists of adding stiffness in parallel to the force sensors. Optimal parallel stiffness is computed.
- Section 5: Relative damping control is applied to the rotating system.
- Section 6: Once the optimal control parameters for the three tested active damping techniques are obtained, they are compared in terms of achievable damping, obtained damped plant and closed-loop compliance and transmissibility.
- Section 7: the previous analysis is applied on three nano-hexapod stiffnesses and optimal active damping controller are obtained.
- Section 8: up until this section, the study was performed on a very simplistic model that just captures the rotation aspect and the model parameters were not tuned to corresponds to the NASS. In this last section, a model of the micro-station is added below the suspended platform (i.e. the nano-hexapod) with a rotating spindle and parameters tuned to match the NASS dynamics. The goal is to determine if the rotation imposes performance limitation for the NASS.

To run the Matlab code, go in the `matlab` directory and run the Matlab files corresponding to each section (see Table 1).

Table 1: Report sections and corresponding Matlab files

Sections	**Matlab File**
Section 1	`rotating_1_system_description.m`
Section 2	`rotating_2_iff_pure_int.m`
Section 3	`rotating_3_iff_hpf.m`
Section 4	`rotating_4_iff_kp.m`
Section 5	`rotating_5_rdc.m`
Section 6	`rotating_5_act_damp_comparison.m`
Section 7	`rotating_6_nano_hexapod.m`
Section 8	`rotating_6_nass.m`

1 System Description and Analysis

The studied system consists of a 2 degree of freedom translation stage on top of a rotating stage (Figure 1.1).

The rotating stage is supposed to be ideal, meaning it induces a perfect rotation $\theta(t) = \Omega t$ where Ω is the rotational speed in $\mathrm{rad\,s^{-1}}$.

The suspended platform consists of two orthogonal actuators each represented by three elements in parallel: a spring with a stiffness k in $\mathrm{N\,m^{-1}}$, a dashpot with a damping coefficient c in N/(m/s) and an ideal force source F_u, F_v. A payload with a mass m in kg, is mounted on the (rotating) suspended platform.

Two reference frames are used: an inertial frame $(\vec{i}_x, \vec{i}_y, \vec{i}_z)$ and a uniform rotating frame $(\vec{i}_u, \vec{i}_v, \vec{i}_w)$ rigidly fixed on top of the rotating stage with $\vec{i}_w$ aligned with the rotation axis. The position of the payload is represented by $(d_u, d_v, 0)$ expressed in the rotating frame.

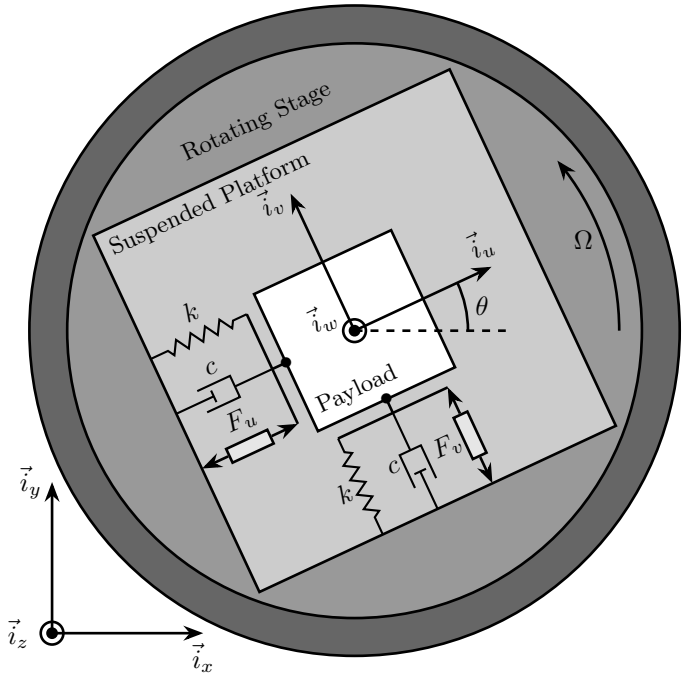

Figure 1.1: Schematic of the studied system

1.1 Equations of motion

To obtain the equations of motion for the system represented in Figure 1.1, the Lagrangian equations are used:

$$\frac{d}{dt}\left(\frac{\partial L}{\partial \dot{q}_i}\right) + \frac{\partial D}{\partial \dot{q}_i} - \frac{\partial L}{\partial q_i} = Q_i \tag{1.1}$$

with $L = T - V$ the Lagrangian, T the kinetic coenergy, V the potential energy, D the dissipation function, and Q_i the generalized force associated with the generalized variable $\begin{bmatrix} q_1 & q_2 \end{bmatrix} = \begin{bmatrix} d_u & d_v \end{bmatrix}$. The equation of motion corresponding to the constant rotation along $\vec{i}_w$ is disregarded as this motion is considered to be imposed by the rotation stage.

$$\begin{aligned} T &= \frac{1}{2} m \left((\dot{d}_u - \Omega d_v)^2 + (\dot{d}_v + \Omega d_u)^2 \right), \\ V &= \frac{1}{2} k \left({d_u}^2 + {d_v}^2 \right), \; Q_1 = F_u, \\ D &= \frac{1}{2} c \left({\dot{d}_u}^2 + {\dot{d}_v}^2 \right), \; Q_2 = F_v \end{aligned} \tag{1.2}$$

Substituting equations (1.2) into equation (1.1) for both generalized coordinates gives two coupled differential equations (1.3a) and (1.3b).

$$m\ddot{d}_u + c\dot{d}_u + (k - m\Omega^2) d_u = F_u + 2m\Omega\dot{d}_v \tag{1.3a}$$

$$m\ddot{d}_v + c\dot{d}_v + (k \underbrace{- m\Omega^2}_{\text{Centrif.}}) d_v = F_v \underbrace{- 2m\Omega\dot{d}_u}_{\text{Coriolis}} \tag{1.3b}$$

The uniform rotation of the system induces **two gyroscopic effects** as shown in equation (1.3):

- **Centrifugal forces**: that can been seen as an added **negative stiffness** $-m\Omega^2$ along $\vec{i}_u$ and $\vec{i}_v$
- **Coriolis Forces**: that adds **coupling** between the two orthogonal directions.

One can verify that without rotation ($\Omega = 0$) the system becomes equivalent to two uncoupled one degree of freedom mass-spring-damper systems.

1.2 Transfer Functions in the Laplace domain

To study the dynamics of the system, the differential equations of motions (1.3) are converted into the Laplace domain and the 2×2 transfer function matrix $\mathbf{G}_d$ from $\begin{bmatrix} F_u & F_v \end{bmatrix}$ to $\begin{bmatrix} d_u & d_v \end{bmatrix}$ in equation (1.4) is obtained. Its elements are shown in equation (1.5).

$$\begin{bmatrix} d_u \\ d_v \end{bmatrix} = \mathbf{G}_d \begin{bmatrix} F_u \\ F_v \end{bmatrix} \tag{1.4}$$

$$\mathbf{G}_d(1,1) = \mathbf{G}_d(2,2) = \frac{ms^2 + cs + k - m\Omega^2}{\left(ms^2 + cs + k - m\Omega^2\right)^2 + (2m\Omega s)^2} \tag{1.5a}$$

$$\mathbf{G}_d(1,2) = -\mathbf{G}_d(2,1) = \frac{2m\Omega s}{\left(ms^2 + cs + k - m\Omega^2\right)^2 + (2m\Omega s)^2} \tag{1.5b}$$

To simplify the analysis, the undamped natural frequency ω_0 and the damping ratio ξ are used as in equation (1.6).

$$\omega_0 = \sqrt{\frac{k}{m}} \text{ in rad s}^{-1}, \quad \xi = \frac{c}{2\sqrt{km}} \tag{1.6}$$

The elements of transfer function matrix $\mathbf{G}_d$ are now described by equation (1.7).

$$\mathbf{G}_d(1,1) = \frac{\frac{1}{k}\left(\frac{s^2}{{\omega_0}^2} + 2\xi\frac{s}{\omega_0} + 1 - \frac{\Omega^2}{{\omega_0}^2}\right)}{\left(\frac{s^2}{{\omega_0}^2} + 2\xi\frac{s}{\omega_0} + 1 - \frac{\Omega^2}{{\omega_0}^2}\right)^2 + \left(2\frac{\Omega}{\omega_0}\frac{s}{\omega_0}\right)^2} \tag{1.7a}$$

$$\mathbf{G}_d(1,2) = \frac{\frac{1}{k}\left(2\frac{\Omega}{\omega_0}\frac{s}{\omega_0}\right)}{\left(\frac{s^2}{{\omega_0}^2} + 2\xi\frac{s}{\omega_0} + 1 - \frac{\Omega^2}{{\omega_0}^2}\right)^2 + \left(2\frac{\Omega}{\omega_0}\frac{s}{\omega_0}\right)^2} \tag{1.7b}$$

1.3 System Poles: Campbell Diagram

The poles of $\mathbf{G}_d$ are the complex solutions p of equation (1.8).

$$\left(\frac{p^2}{{\omega_0}^2} + 2\xi\frac{p}{\omega_0} + 1 - \frac{\Omega^2}{{\omega_0}^2}\right)^2 + \left(2\frac{\Omega}{\omega_0}\frac{p}{\omega_0}\right)^2 = 0 \tag{1.8}$$

Supposing small damping ($\xi \ll 1$), two pairs of complex conjugate poles are obtained as shown in equation (1.9).

$$p_+ = -\xi\omega_0\left(1 + \frac{\Omega}{\omega_0}\right) \pm j\omega_0\left(1 + \frac{\Omega}{\omega_0}\right) \tag{1.9a}$$

$$p_- = -\xi\omega_0\left(1 - \frac{\Omega}{\omega_0}\right) \pm j\omega_0\left(1 - \frac{\Omega}{\omega_0}\right) \tag{1.9b}$$

The real and complex parts of these two pairs of complex conjugate poles are represented in Figure 1.2 as a function of the rotational speed Ω. As the rotational speed increases, p_+ goes to higher frequencies and p_- goes to lower frequencies. The system becomes unstable for $\Omega > \omega_0$ as the real part of p_- is positive. Physically, the negative stiffness term $-m\Omega^2$ induced by centrifugal forces exceeds the spring stiffness k.

1.4 System Dynamics: Effect of rotation

The system dynamics from actuator forces $[F_u, F_v]$ to the relative motion $[d_u, d_v]$ is identified for several rotating velocities.

Looking at the transfer function matrix $\mathbf{G}_d$ in equation (1.7), one can see that the two diagonal (direct) terms are equal and that the two off-diagonal (coupling) terms are opposite. The bode plot of these

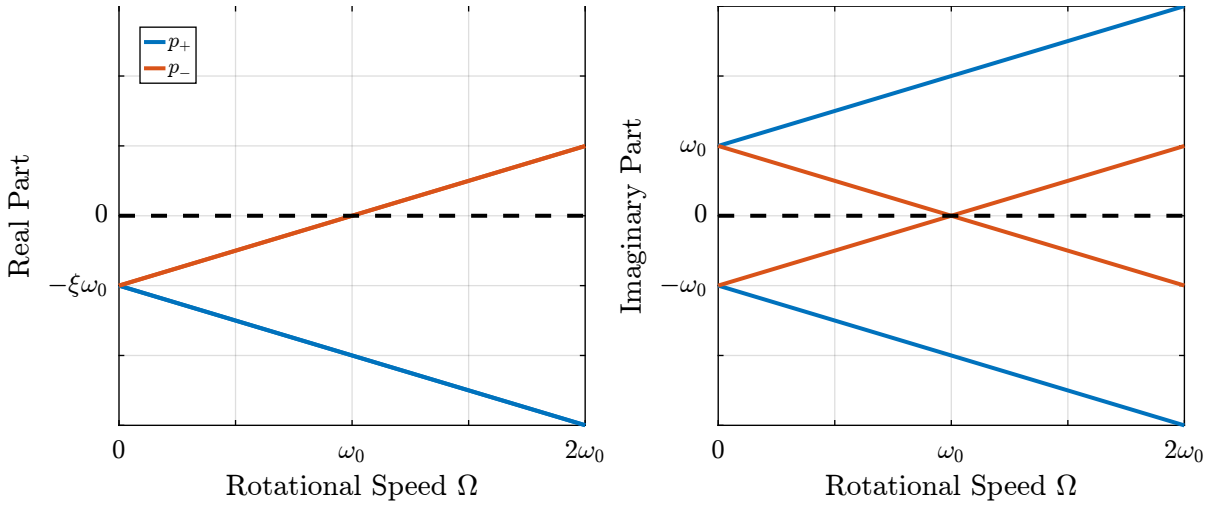

Figure 1.2: Campbell diagram - Real and Imaginary parts of the poles as a function of the rotating velocity

two terms are shown in Figure 1.3 for several rotational speeds Ω. These plots confirm the expected behavior: the frequency of the two pairs of complex conjugate poles are further separated as Ω increases. For $\Omega > \omega_0$, the low frequency pair of complex conjugate poles p_- becomes unstable.

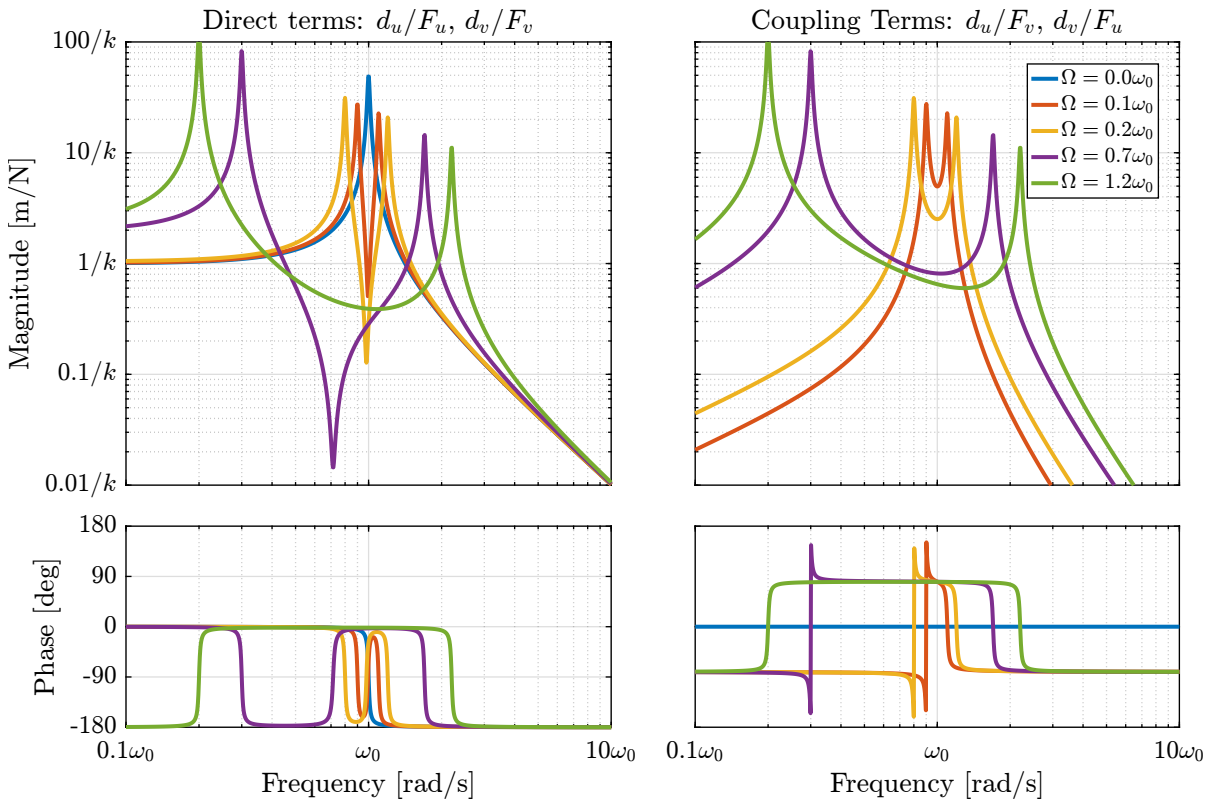

Figure 1.3: Bode plot of the direct and coupling terms for several rotating velocities

2 Integral Force Feedback

In order to further decrease the residual vibrations, active damping can be used for reducing the magnification of the response in the vicinity of the resonances [1].

Many active damping techniques have been developed over the years such as Positive Position Feedback (PPF) [2, 3], Integral Force Feedback (IFF) [4] and Direct Velocity Feedback (DVF) [5–7].

In [8], the IFF control scheme has been proposed, where a force sensor, a force actuator and an integral controller are used to directly augment the damping of a mechanical system. When the force sensor is collocated with the actuator, the open-loop transfer function has alternating poles and zeros which facilitate to guarantee the stability of the closed loop system [7]. It was latter shown that this property holds for multiple collated actuator/sensor pairs [9].

The main advantages of IFF over other active damping techniques are the guaranteed stability even in presence of flexible dynamics, good performances and robustness properties [7].

Several improvements of the classical IFF have been proposed, such as adding a feed-through term to increase the achievable damping [10] or adding an high pass filter to recover the loss of compliance at low frequency [11]. Recently, an $\mathcal{H}_\infty$ optimization criterion has been used to derive optimal gains for the IFF controller [12].

However, none of these study have been applied to a rotating system. In this section, Integral Force Feedback strategy is applied on the rotating suspended platform, and it is shown that gyroscopic effects alters the system dynamics and that IFF cannot be applied as is.

2.1 System and Equations of motion

In order to apply Integral Force Feedback, two force sensors are added in series with the actuators (Figure 2.1). Two identical controllers K_F are then used to feedback each of the sensed force to its associated actuator:

$$K_F(s) = g \cdot \frac{1}{s} \tag{2.1}$$

The forces $\begin{bmatrix} f_u & f_v \end{bmatrix}$ measured by the two force sensors represented in Figure 2.1 are described by equation (2.2).

$$\begin{bmatrix} f_u \\ f_v \end{bmatrix} = \begin{bmatrix} F_u \\ F_v \end{bmatrix} - (cs + k) \begin{bmatrix} d_u \\ d_v \end{bmatrix} \tag{2.2}$$

The transfer function matrix $\mathbf{G}_f$ from actuator forces to measured forces in equation (2.3) can be obtained by inserting equation (1.7) into equation (2.2). Its elements are shown in equation (2.4).

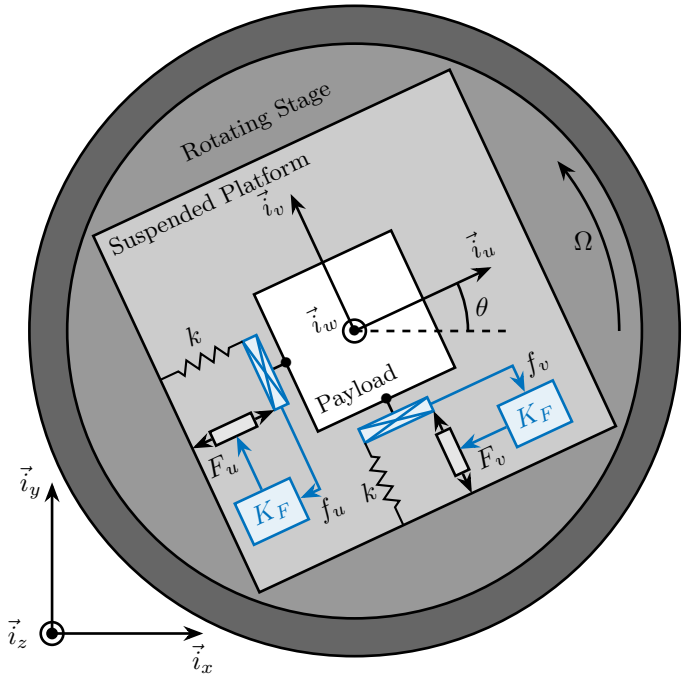

Figure 2.1: System with added Force Sensor in series with the actuators (shown in blue with the associated controllers)

$$\begin{bmatrix} f_u \\ f_v \end{bmatrix} = \mathbf{G}_f \begin{bmatrix} F_u \\ F_v \end{bmatrix} \tag{2.3}$$

$$\mathbf{G}_f(1,1) = \mathbf{G}_f(2,2) = \frac{\left(\frac{s^2}{{\omega_0}^2} - \frac{\Omega^2}{{\omega_0}^2}\right)\left(\frac{s^2}{{\omega_0}^2} + 2\xi\frac{s}{\omega_0} + 1 - \frac{\Omega^2}{{\omega_0}^2}\right) + \left(2\frac{\Omega}{\omega_0}\frac{s}{\omega_0}\right)^2}{\left(\frac{s^2}{{\omega_0}^2} + 2\xi\frac{s}{\omega_0} + 1 - \frac{\Omega^2}{{\omega_0}^2}\right)^2 + \left(2\frac{\Omega}{\omega_0}\frac{s}{\omega_0}\right)^2} \tag{2.4a}$$

$$\mathbf{G}_f(1,2) = -\mathbf{G}_f(2,1) = \frac{-\left(2\xi\frac{s}{\omega_0} + 1\right)\left(2\frac{\Omega}{\omega_0}\frac{s}{\omega_0}\right)}{\left(\frac{s^2}{{\omega_0}^2} + 2\xi\frac{s}{\omega_0} + 1 - \frac{\Omega^2}{{\omega_0}^2}\right)^2 + \left(2\frac{\Omega}{\omega_0}\frac{s}{\omega_0}\right)^2} \tag{2.4b}$$

The zeros of the diagonal terms of $\mathbf{G}_f$ in equation (2.4a) are computed, and neglecting the damping for simplicity, **two complex conjugated zeros** z_c are obtained in equation (2.5a), and **two real zeros** z_r in equation (2.5b).

$$z_c = \pm j\omega_0\sqrt{\frac{1}{2}\sqrt{8\frac{\Omega^2}{{\omega_0}^2} + 1} + \frac{\Omega^2}{{\omega_0}^2} + \frac{1}{2}} \tag{2.5a}$$

$$z_r = \pm\omega_0\sqrt{\frac{1}{2}\sqrt{8\frac{\Omega^2}{{\omega_0}^2} + 1} - \frac{\Omega^2}{{\omega_0}^2} - \frac{1}{2}} \tag{2.5b}$$

It is interesting to see that the frequency of the pair of complex conjugate zeros z_c in equation (2.5a) always lies between the frequency of the two pairs of complex conjugate poles p_- and p_+ in equation

(1.9). This is what usually gives the unconditional stability of IFF when collocated force sensors are used.

However, for non-null rotational speeds, the two real zeros z_r in equation (2.5b) are inducing a **non-minimum phase behavior**. This can be seen in the Bode plot of the diagonal terms (Figure 2.2) where the low frequency gain is no longer zero while the phase stays at 180°.

The low frequency gain of $\mathbf{G}_f$ increases with the rotational speed Ω as shown in equation (2.6).

$$\lim_{\omega \to 0} |\mathbf{G}_f(j\omega)| = \begin{bmatrix} \frac{\Omega^2}{{\omega_0}^2 - \Omega^2} & 0 \\ 0 & \frac{\Omega^2}{{\omega_0}^2 - \Omega^2} \end{bmatrix} \tag{2.6}$$

This can be explained as follows: a constant actuator force F_u induces a small displacement of the mass $d_u = \frac{F_u}{k - m\Omega^2}$ (Hooke's law taking into account the negative stiffness induced by the rotation). This small displacement then increases the centrifugal force $m\Omega^2 d_u = \frac{\Omega^2}{{\omega_0}^2 - \Omega^2} F_u$ which is then measured by the force sensors.

2.2 Effect of the rotation speed on the IFF plant dynamics

The transfer functions from actuator forces $[F_u,\ F_v]$ to the measured force sensors $[f_u,\ f_v]$ are identified for several rotating velocities and shown in Figure 2.2.

As was expected from the derived equations of motion:

- when $0 < \Omega < \omega_0$: the low frequency gain is no longer zero and two (non-minimum phase) real zero appears at low frequency. The low frequency gain increases with Ω. A pair of (minimum phase) complex conjugate zeros appears between the two complex conjugate poles that are split further apart as Ω increases.
- when $\omega_0 < \Omega$: the low frequency pole becomes unstable.

2.3 Decentralized Integral Force Feedback

The control diagram for decentralized Integral Force Feedback is shown in Figure 2.3.

The decentralized IFF controller $\boldsymbol{K}_F$ corresponds to a diagonal controller with integrators:

$$\begin{aligned} \mathbf{K}_F(s) &= \begin{bmatrix} K_F(s) & 0 \\ 0 & K_F(s) \end{bmatrix} \\ K_F(s) &= g \cdot \frac{1}{s} \end{aligned} \tag{2.7}$$

In order to see how the IFF controller affects the poles of the closed loop system, a Root Locus plot (Figure 2.4) is constructed as follows: the poles of the closed-loop system are drawn in the complex plane as the controller gain g varies from 0 to ∞ for the two controllers K_F simultaneously. As explained

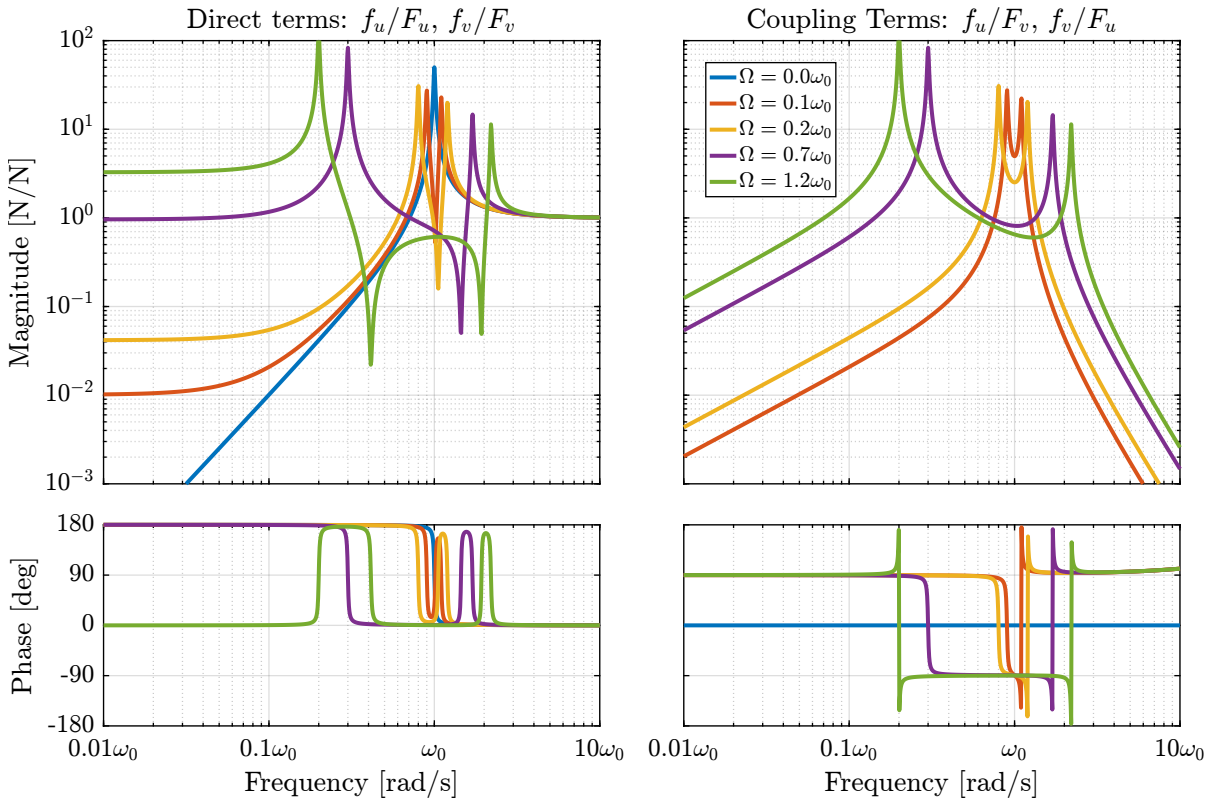

Figure 2.2: Bode plot of the direct and coupling term for Integral Force Feedback - Effect of rotation

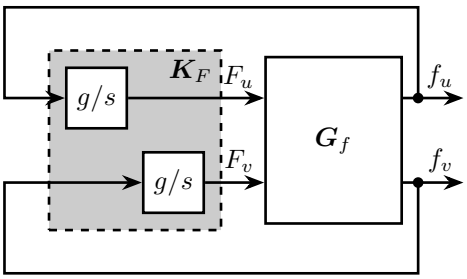

Figure 2.3: Control diagram for decentralized Integral Force Feedback

in [9, 13], the closed-loop poles start at the open-loop poles (shown by ✖) for $g = 0$ and coincide with the transmission zeros (shown by ⭘) as $g \to \infty$.

Important

Whereas collocated IFF is usually associated with unconditional stability [4], this property is lost due to gyroscopic effects as soon as the rotation velocity in non-null. This can be seen in the Root Locus plot (Figure 2.4) where poles corresponding to the controller are bound to the right half plane implying closed-loop system instability.

Physically, this can be explained like so: at low frequency, the loop gain is very large due to the pure integrator in K_F and the finite gain of the plant (Figure 2.2). The control system is thus canceling the spring forces which makes the suspended platform no able to hold the payload against centrifugal forces, hence the instability.

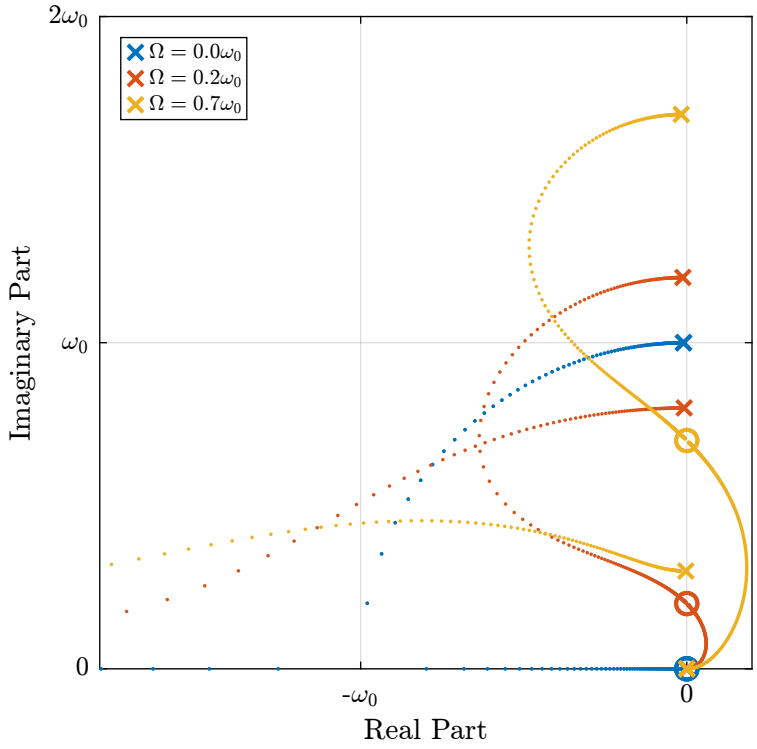

Figure 2.4: Root Locus for the Decentralized Integral Force Feedback controller. Several rotating speed are shown.

3 Integral Force Feedback with an High Pass Filter

As was explained in the previous section, the instability of the IFF controller applied on the rotating system comes in part from the high gain at low frequency caused by the pure integrators.

In order to limit the low frequency controller gain, an High Pass Filter (HPF) can be added to the controller as shown in equation (3.1).

$$K_F(s) = g \cdot \frac{1}{s} \cdot \underbrace{\frac{s/\omega_i}{1 + s/\omega_i}}_{\text{HPF}} = g \cdot \frac{1}{s+\omega_i} \tag{3.1}$$

This is equivalent as to slightly **shifting the controller pole to the left along the real axis**.

This modification of the IFF controller is typically done to avoid saturation associated with the pure integrator [4, 14]. This is however not why this high pass filter is added here.

3.1 Modified Integral Force Feedback Controller

The Integral Force Feedback Controller is modified such that instead of using pure integrators, pseudo integrators (i.e. low pass filters) are used:

$$K_{\text{IFF}}(s) = g \frac{1}{\omega_i + s} \begin{bmatrix} 1 & 0 \\ 0 & 1 \end{bmatrix} \tag{3.2}$$

where ω_i characterize down to which frequency the signal is integrated.

Let's arbitrary choose the following control parameters:

Matlab
```
%% Modified IFF - parameters
g = 2; % Controller gain
wi = 0.1; % HPF Cut-Off frequency [rad/s]

Kiff     = (g/s)*eye(2); % Pure IFF
Kiff_hpf = (g/(wi+s))*eye(2); % IFF with added HPF
```

The loop gains ($K_F(s)$ times the direct dynamics f_u/F_u) with and without the added HPF are shown in Figure 3.1. The effect of the added HPF limits the low frequency gain to finite values as expected.

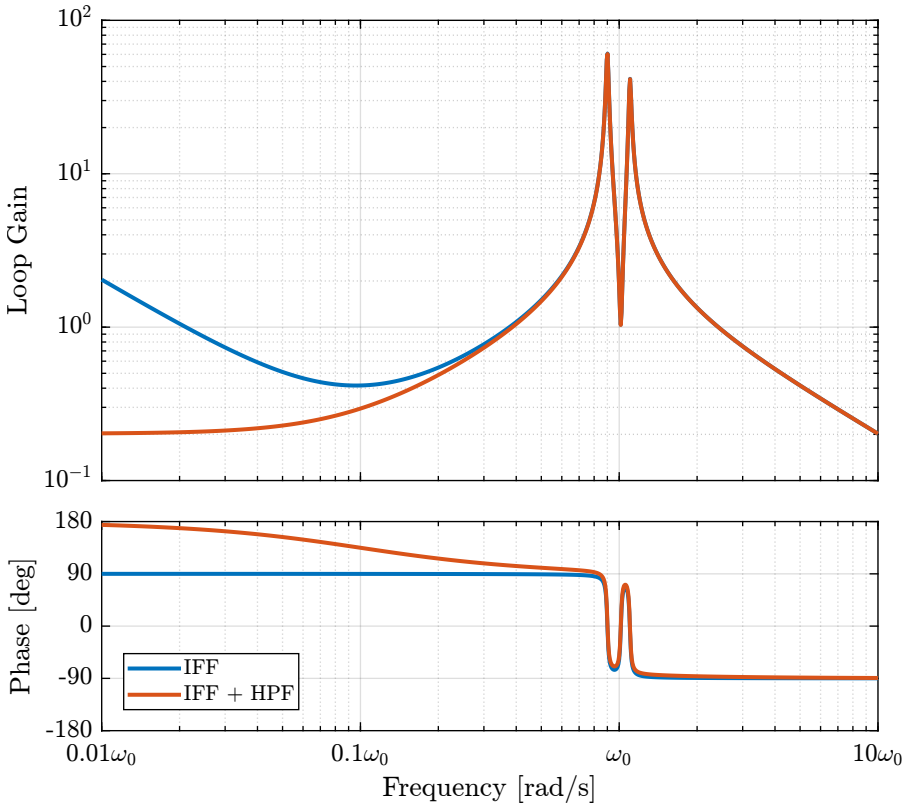

Figure 3.1: Loop gain for the IFF with pure integrator and modified IFF with added high pass filter ($\Omega = 0.1\omega_0$)

The Root Locus plots for the decentralized IFF with and without the HPF are displayed in Figure 3.2. With the added HPF, the poles of the closed loop system are shown to be **stable up to some value of the gain** $g_{\max}$ given by equation (3.3).

$$g_{\max} = \omega_i \left(\frac{{\omega_0}^2}{\Omega^2} - 1 \right) \tag{3.3}$$

It is interesting to note that $g_{\max}$ also corresponds to the controller gain at which the low frequency loop gain (Figure 3.1) reaches one.

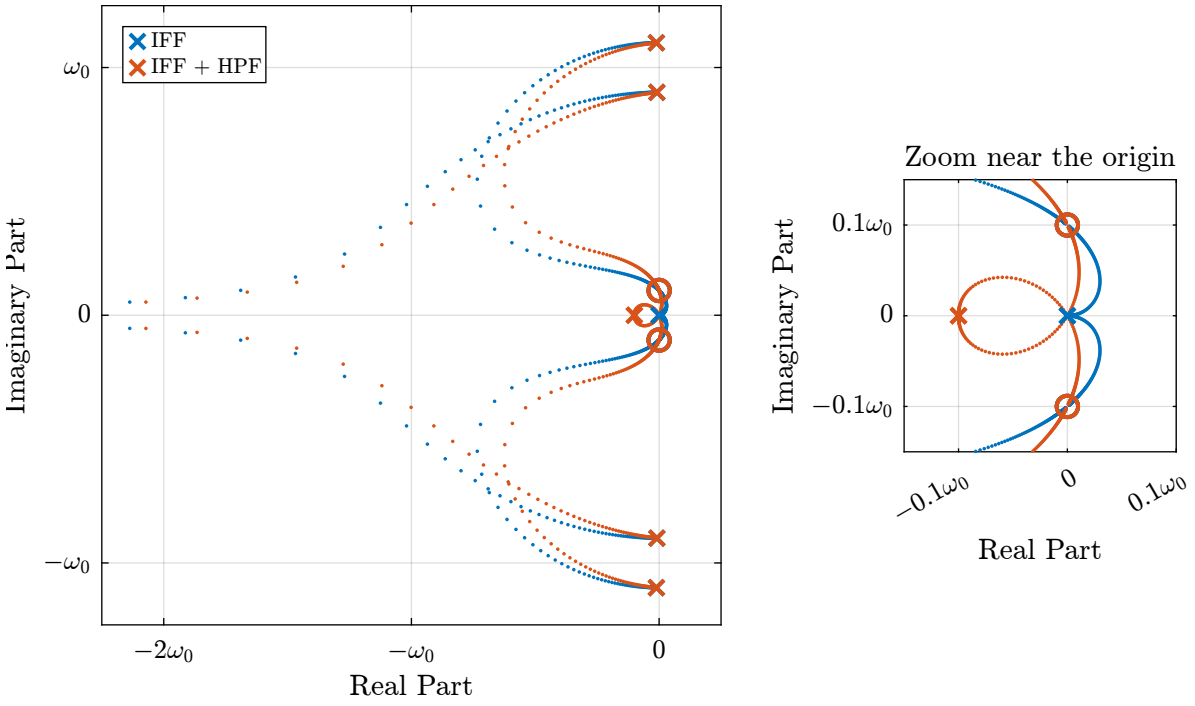

Figure 3.2: Root Locus for the initial IFF and the modified IFF

3.2 Optimal IFF with HPF parameters ω_i and g

Two parameters can be tuned for the modified controller in equation (3.1): the gain g and the pole's location ω_i. The optimal values of ω_i and g are here considered as the values for which the damping of all the closed-loop poles are simultaneously maximized.

In order to visualize how ω_i does affect the attainable damping, the Root Locus plots for several ω_i are displayed in Figure 3.3. It is shown that even though small ω_i seem to allow more damping to be added to the suspension modes, the control gain g may be limited to small values due to equation (3.3).

In order to study this trade off, the attainable closed-loop damping ratio ξ_{cl} is computed as a function of ω_i/ω_0. The gain g_{opt} at which this maximum damping is obtained is also displayed and compared with the gain $g_{\max}$ at which the system becomes unstable (Figure 3.4).

Three regions can be observed:

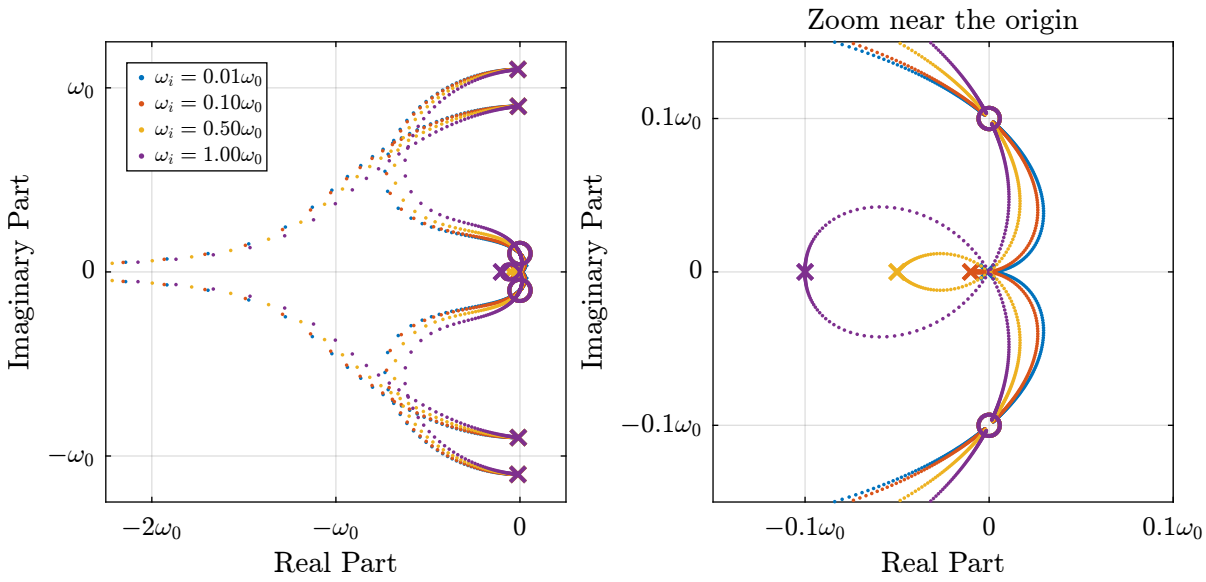

Figure 3.3: Root Locus for several high pass filter cut-off frequency

- $\omega_i/\omega_0 < 0.02$: the added damping is limited by the maximum allowed control gain $g_{\max}$
- $0.02 < \omega_i/\omega_0 < 0.2$: the attainable damping ratio is maximized and is reached for $g \approx 2$
- $0.2 < \omega_i/\omega_0$: the added damping decreases as ω_i/ω_0 increases.

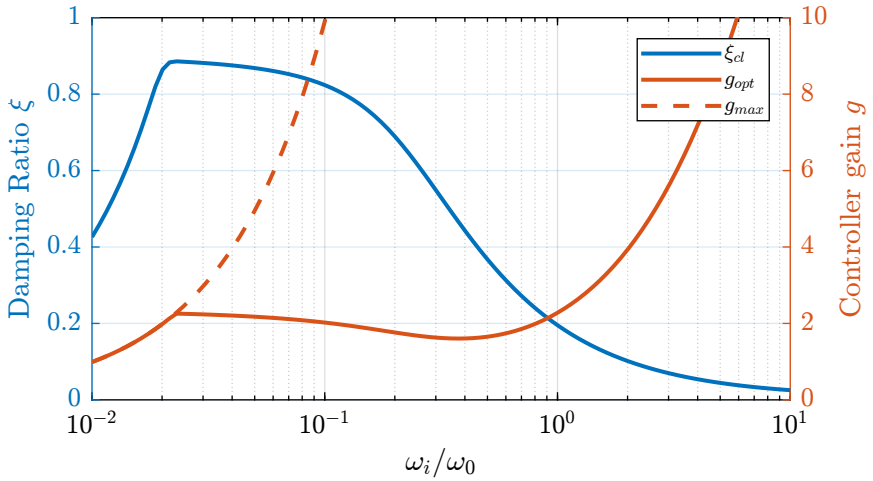

Figure 3.4: Attainable damping ratio ξ_{cl} as a function of ω_i/ω_0. Corresponding control gain g_{opt} and $g_{\max}$ are also shown

3.3 Obtained Damped Plant

Let's choose $\omega_i = 0.1 \cdot \omega_0$ and compute the damped plant. The undamped and damped plants are compared in Figure 3.5 in blue and red respectively. A well damped plant is indeed obtained.

However, the magnitude of the coupling term (d_v/F_u) is larger then IFF is applied.

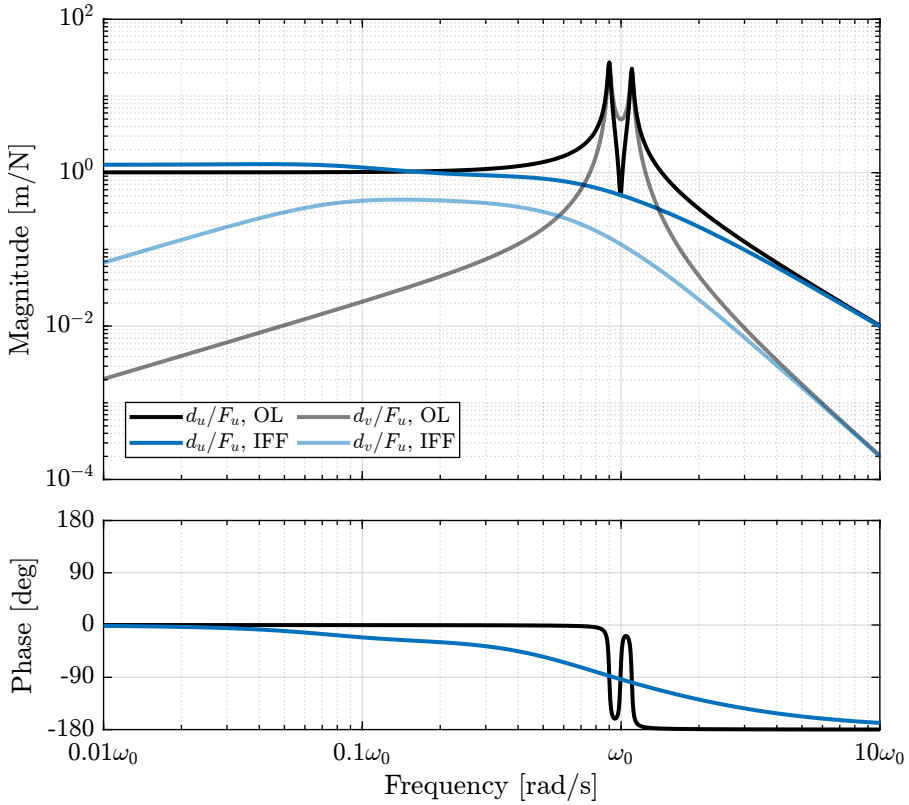

Figure 3.5: Damped plant with IFF and added HPF - Transfer function from F_u to d_u, $\omega_i = 0.1 \cdot \omega_0$, $\Omega = 0.1 \cdot \omega_0$

In order to study how ω_i affects the coupling of the damped plant, the closed-loop plant is identified for several ω_i. The direct and coupling terms of the plants are shown in Figure 3.6 (left) and the ratio between the two (i.e. the coupling ratio) is shown in Figure 3.6 (right).

The coupling ratio is decreasing as ω_i increases. There is therefore a **trade-off between achievable damping and coupling ratio** for the choice of ω_i. The same trade-off can be seen between achievable damping and loss of compliance at low frequency (see Figure 3.7).

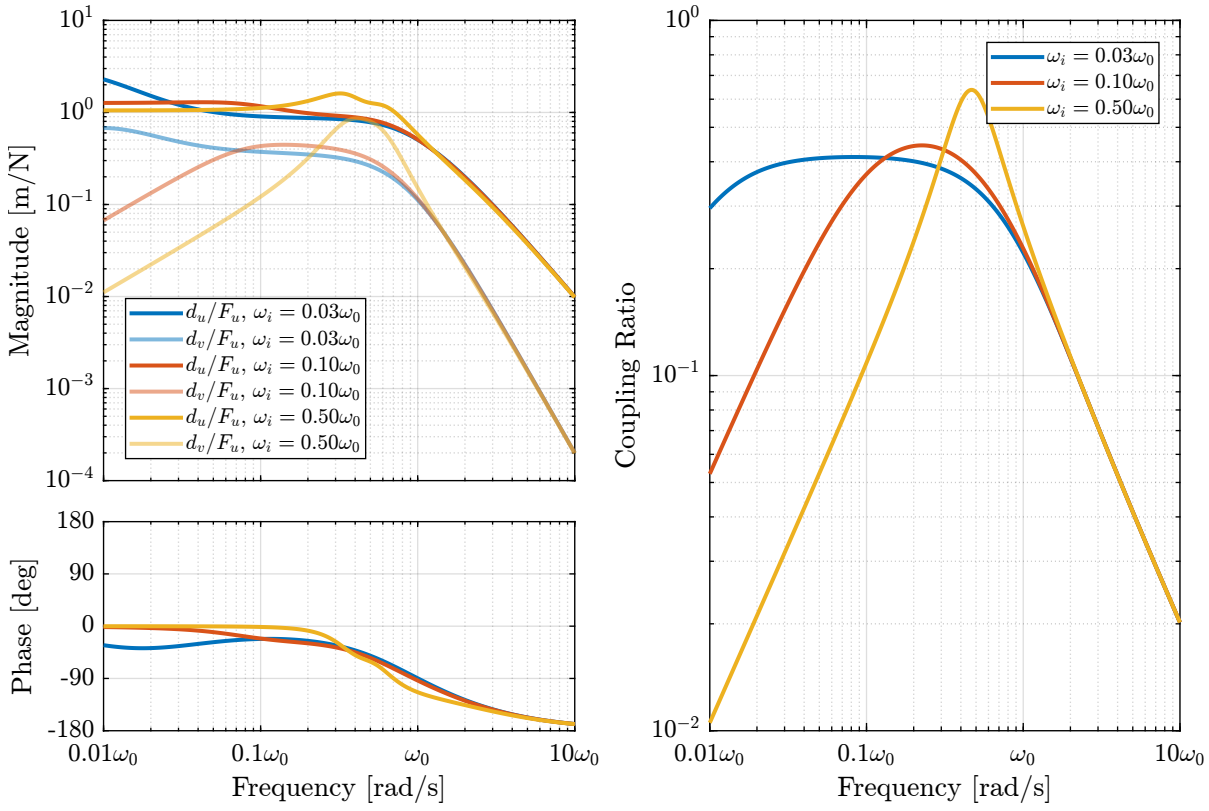

Figure 3.6: Effect of ω_i on the damped plant coupling

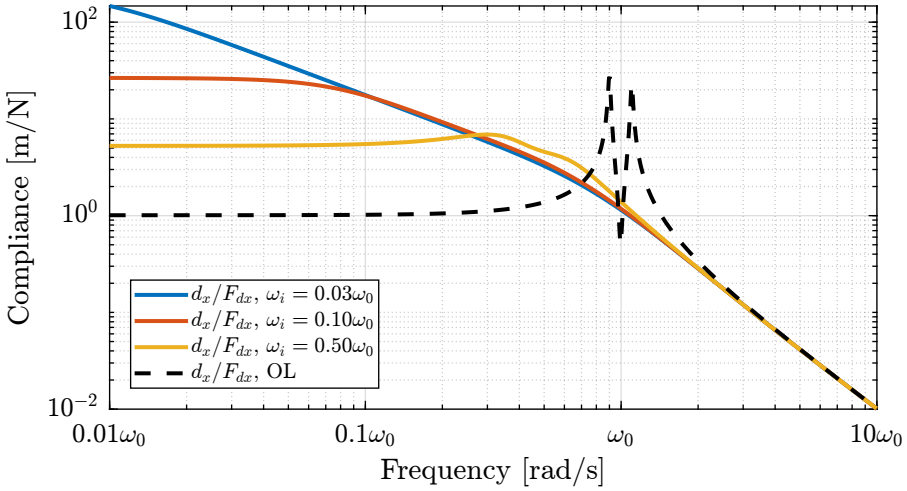

Figure 3.7: Effect of ω_i on the obtained compliance

4 IFF with a stiffness in parallel with the force sensor

In this section it is proposed to add springs in parallel with the force sensors to counteract the negative stiffness induced by the gyroscopic effects.

Such springs are schematically shown in Figure 4.1 where k_a is the stiffness of the actuator and k_p the added stiffness in parallel with the actuator and force sensor.

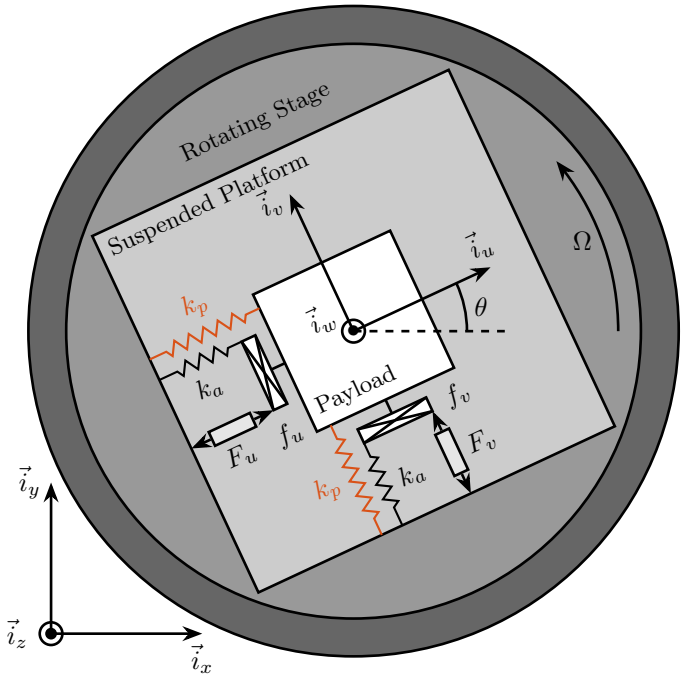

Figure 4.1: Studied system with additional springs in parallel with the actuators and force sensors (shown in red)

4.1 Equations

The forces measured by the two force sensors represented in Figure 4.1 are described by Eq. (4.1).

$$\begin{bmatrix} f_u \\ f_v \end{bmatrix} = \begin{bmatrix} F_u \\ F_v \end{bmatrix} - (cs + k_a) \begin{bmatrix} d_u \\ d_v \end{bmatrix} \tag{4.1}$$

In order to keep the overall stiffness $k = k_a + k_p$ constant, thus not modifying the open-loop poles as k_p is changed, a scalar parameter α ($0 \leq \alpha < 1$) is defined to describe the fraction of the total stiffness in parallel with the actuator and force sensor as in Eq. (4.2).

$$k_p = \alpha k, \quad k_a = (1-\alpha)k \tag{4.2}$$

After the equations of motion derived and transformed in the Laplace domain, the transfer function matrix $\mathbf{G}_k$ in Eq. (4.3) is computed. Its elements are shown in Eq. (4.4a) and (4.4b).

$$\begin{bmatrix} f_u \\ f_v \end{bmatrix} = \mathbf{G}_k \begin{bmatrix} F_u \\ F_v \end{bmatrix} \tag{4.3}$$

$$\mathbf{G}_k(1,1) = \mathbf{G}_k(2,2) = \frac{\left(\frac{s^2}{{\omega_0}^2} - \frac{\Omega^2}{{\omega_0}^2} + \alpha\right)\left(\frac{s^2}{{\omega_0}^2} + 2\xi\frac{s}{\omega_0} + 1 - \frac{\Omega^2}{{\omega_0}^2}\right) + \left(2\frac{\Omega}{\omega_0}\frac{s}{\omega_0}\right)^2}{\left(\frac{s^2}{{\omega_0}^2} + 2\xi\frac{s}{\omega_0} + 1 - \frac{\Omega^2}{{\omega_0}^2}\right)^2 + \left(2\frac{\Omega}{\omega_0}\frac{s}{\omega_0}\right)^2} \tag{4.4a}$$

$$\mathbf{G}_k(1,2) = -\mathbf{G}_k(2,1) = \frac{-\left(2\xi\frac{s}{\omega_0} + 1 - \alpha\right)\left(2\frac{\Omega}{\omega_0}\frac{s}{\omega_0}\right)}{\left(\frac{s^2}{{\omega_0}^2} + 2\xi\frac{s}{\omega_0} + 1 - \frac{\Omega^2}{{\omega_0}^2}\right)^2 + \left(2\frac{\Omega}{\omega_0}\frac{s}{\omega_0}\right)^2} \tag{4.4b}$$

Comparing $\mathbf{G}_k$ in Eq. (4.4) with $\mathbf{G}_f$ in Eq. (2.4) shows that while the poles of the system are kept the same, the zeros of the diagonal terms have changed. The two real zeros z_r in Eq. (2.5b) that were inducing a non-minimum phase behavior are transformed into two complex conjugate zeros if the condition in Eq. (4.5) holds.

$$\boxed{\alpha > \frac{\Omega^2}{{\omega_0}^2} \quad \Leftrightarrow \quad k_p > m\Omega^2} \tag{4.5}$$

Important

Thus, if the added **parallel stiffness** k_p is **higher than the negative stiffness induced by centrifugal forces** $m\Omega^2$, the dynamics from actuator to its collocated force sensor will show minimum phase behavior.

4.2 Effect of the parallel stiffness on the IFF plant

The IFF plant (transfer function from $[F_u, F_v]$ to $[f_u, f_v]$) is identified in three different cases:

- without parallel stiffness $k_p = 0$
- with a small parallel stiffness $k_p < m\Omega^2$
- with a large parallel stiffness $k_p > m\Omega^2$

The Bode plots of the obtained dynamics are shown in Figure 4.2. One can see that for $k_p > m\Omega^2$, the two real zeros with $k_p < m\Omega^2$ are transformed into two complex conjugate zeros and the systems shows alternating complex conjugate poles and zeros.

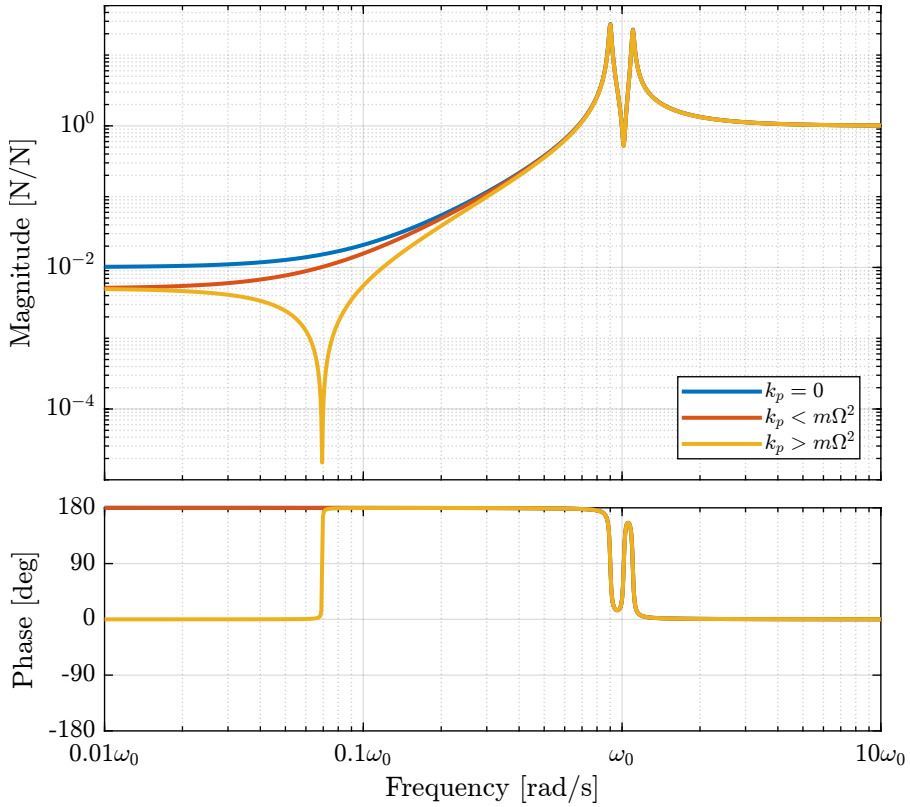

Figure 4.2: Effect of the parallel stiffness on the IFF plant: Bode plot of $G_k(1,1) = f_u/F_u$ without parallel spring, with parallel spring stiffness $k_p < m\Omega^2$ and $k_p > m\Omega^2$, $\Omega = 0.1\omega_0$

Figure 4.3 shows the Root Locus plots for $k_p = 0$, $k_p < m\Omega^2$ and $k_p > m\Omega^2$ when K_F is a pure integrator as in Eq. (2.7). It is shown that if the added stiffness is higher than the maximum negative stiffness, the poles of the closed-loop system are bounded on the (stable) left half-plane, and hence the **unconditional stability of IFF is recovered**.

4.3 Effect of k_p on the attainable damping

Even though the parallel stiffness k_p has no impact on the open-loop poles (as the overall stiffness k is kept constant), it has a large impact on the transmission zeros. Moreover, as the attainable damping is generally proportional to the distance between poles and zeros [15], the parallel stiffness k_p is foreseen to have some impact on the attainable damping.

To study this effect, Root Locus plots for several parallel stiffnesses $k_p > m\Omega^2$ are shown in Figure 4.4. The frequencies of the transmission zeros of the system are increasing with an increase of the parallel stiffness k_p (thus getting closer to the poles) and the associated attainable damping is reduced.

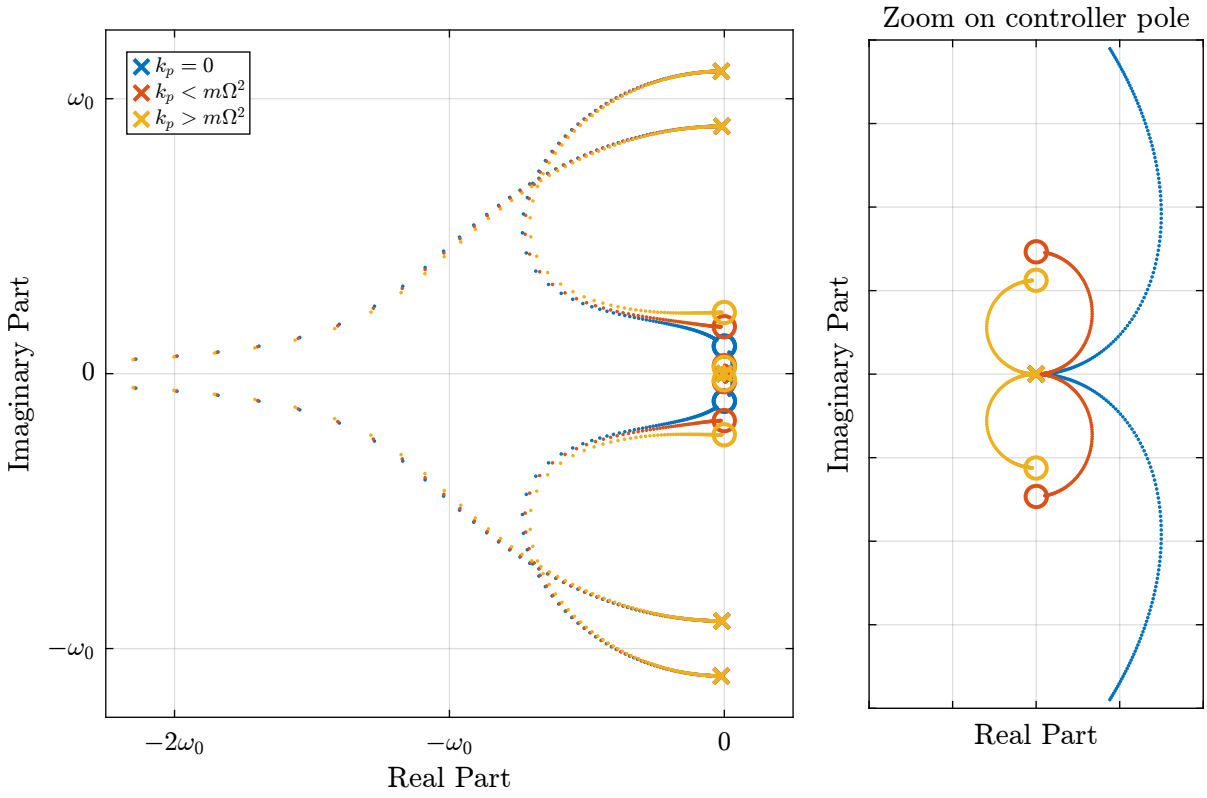

Figure 4.3: Root Locus for IFF without parallel spring, with small parallel spring and with large parallel spring

Important

Therefore, even though the parallel stiffness k_p should be larger than $m\Omega^2$ for stability reasons, it should not be taken too large as this would limit the attainable damping.

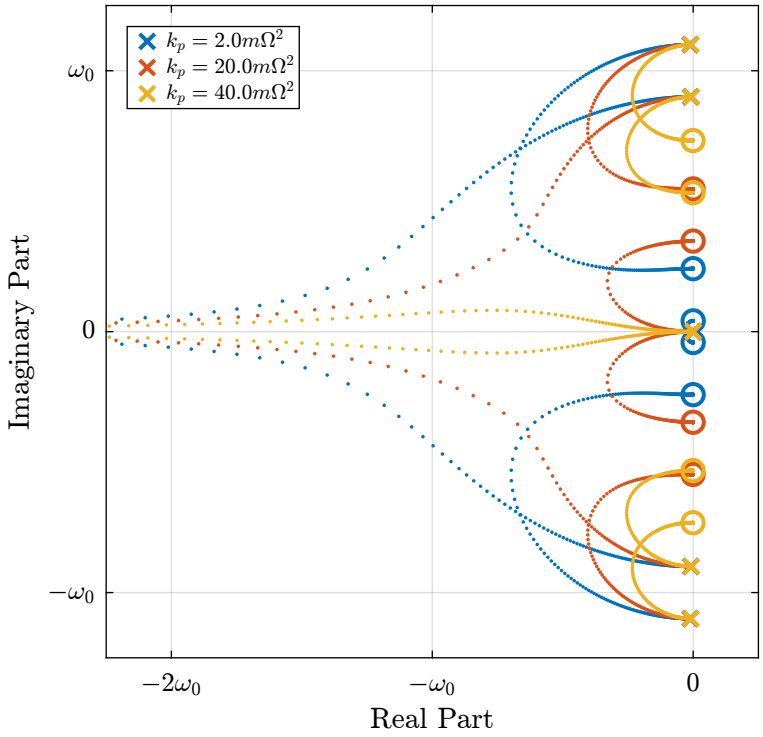

Figure 4.4: Root Locus: Effect of the parallel stiffness on the attainable damping, $\Omega = 0.1\omega_0$

This is confirmed by the Figure 4.5 where the attainable closed-loop damping ratio ξ_{cl} and the associated optimal control gain g_{opt} are computed as a function of the parallel stiffness.

4.4 Damped plant

Let's choose a parallel stiffness equal to $k_p = 2m\Omega^2$ and compute the damped plant. The damped and undamped transfer functions from F_u to d_u are compared in Figure 4.6.

Even though the two resonances are well damped, the IFF changes the low frequency behavior of the plant which is usually not wanted. This is due to the fact that "pure" integrators are used, and that the low frequency loop gains becomes large below some frequency.

In order to lower the low frequency gain, an high pass filter is added to the IFF controller (which is equivalent as shifting the controller pole to the left in the complex plane):

$$K_{\text{IFF}}(s) = g\frac{1}{\omega_i + s}\begin{bmatrix} 1 & 0 \\ 0 & 1 \end{bmatrix} \tag{4.6}$$

Let's see how the high pass filter impacts the attainable damping. The controller gain g is kept constant while ω_i is changed, and the minimum damping ratio of the damped plant is computed. The obtained

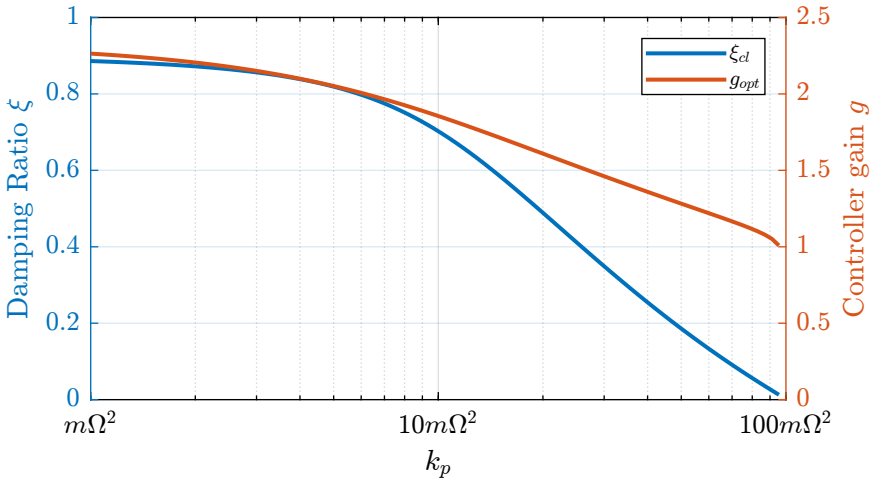

Figure 4.5: Attainable damping ratio ξ_{cl} as a function of the parallel stiffness k_p. Corresponding control gain g_{opt} is also shown. Values for $k_p < m\Omega^2$ are not shown as the system is unstable.

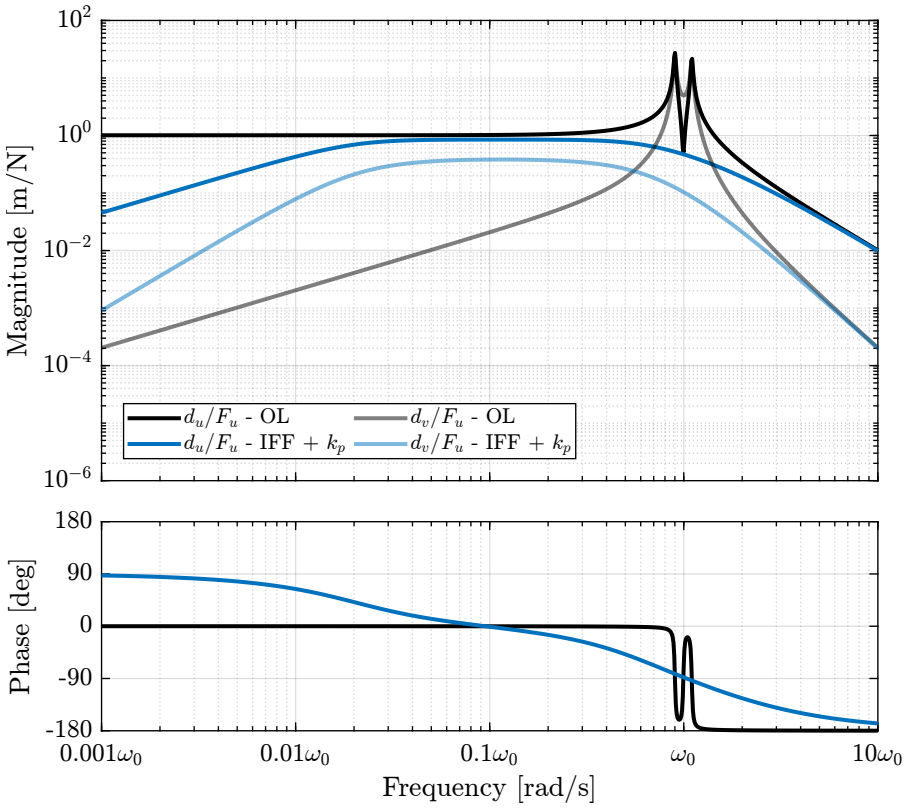

Figure 4.6: Damped plant with IFF - Transfer function from F_u to d_u

damping ratio as a function of ω_i/ω_0 (where ω_0 is the resonance of the system without rotation) is shown in Figure 4.7.

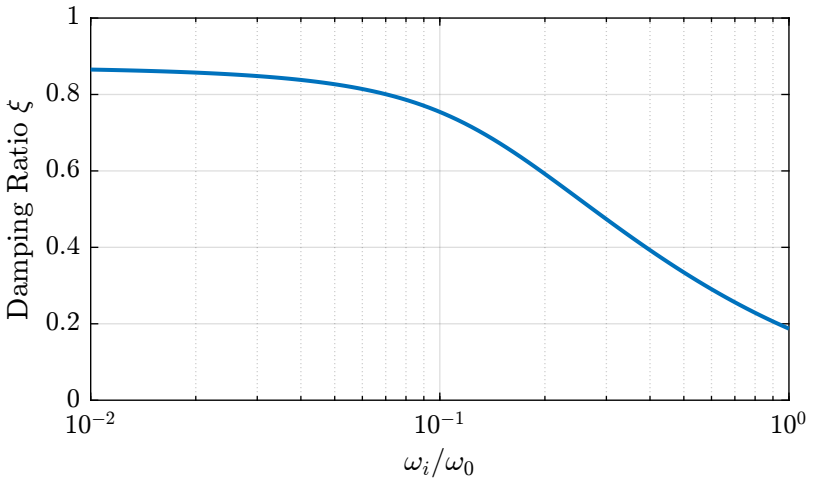

Figure 4.7: Effect of the high pass filter cut-off frequency on the obtained damping

Let's choose $\omega_i = 0.1 \cdot \omega_0$ and compute the damped plant again. The Bode plots of the undamped, damped with "pure" IFF, and with added high pass filters are shown in Figure 4.8. The added high pass filter gives almost the same damping properties while giving acceptable low frequency behavior.

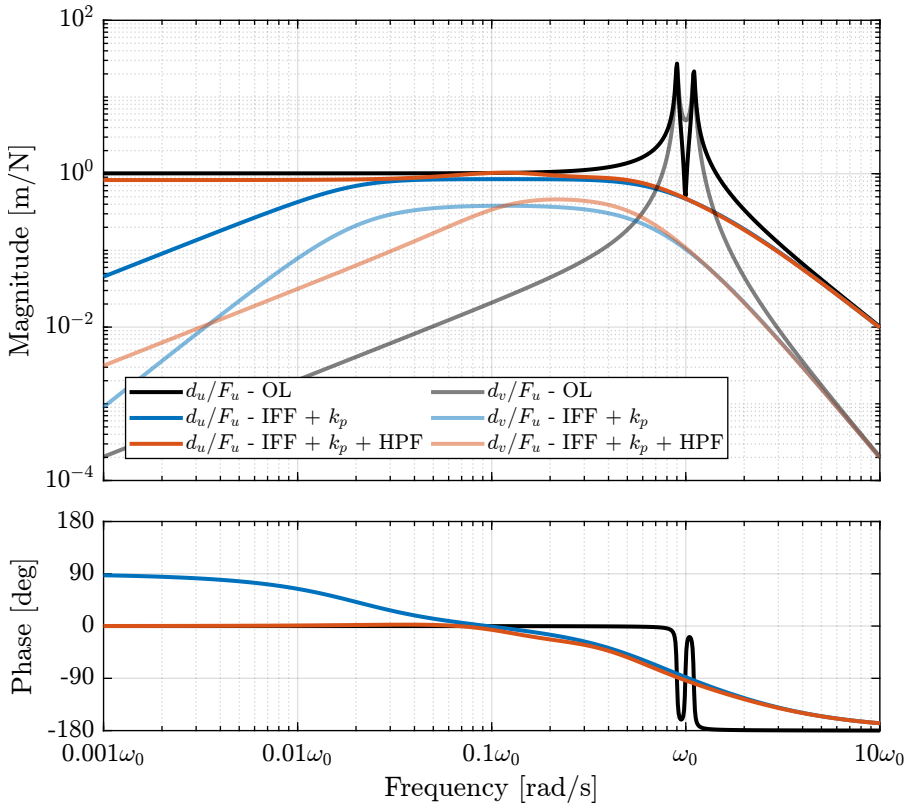

Figure 4.8: Damped plant with IFF - Transfer function from F_u to d_u

5 Relative Damping Control

In order to apply a "relative damping control strategy", relative motion sensors are added in parallel with the actuators as shown in Figure 5.1.

Two controllers K_d are used to fed back the relative motion to the actuator. K_d is a derivator:

$$K_d(s) = s \tag{5.1}$$

To be implemented in practice, it is usually replaced by a an high pass filter:

$$K_d(s) = \frac{s}{s + \omega_d} \tag{5.2}$$

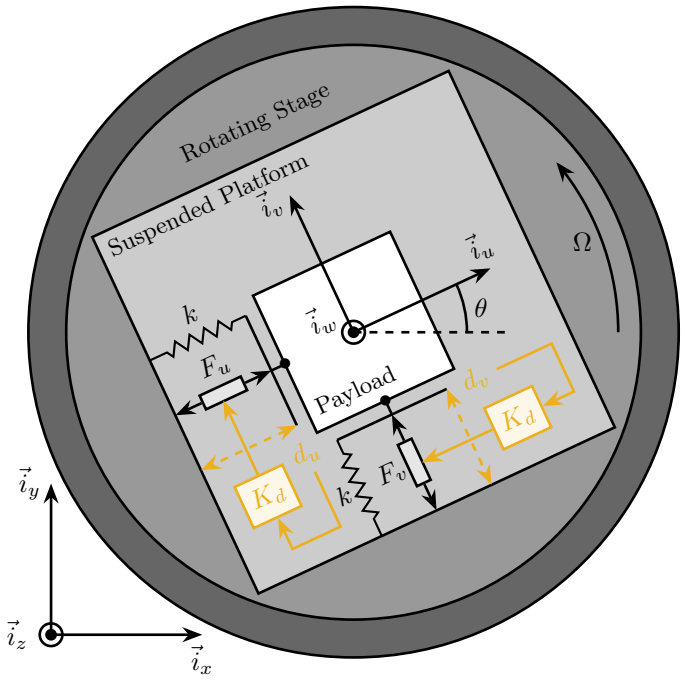

Figure 5.1: System with relative motion sensor and decentralized "relative damping control" applied.

5.1 Equations of motion

Let's note $\boldsymbol{G}_d$ the transfer function between actuator forces and measured relative motion in parallel with the actuators:

$$\begin{bmatrix} d_u \\ d_v \end{bmatrix} = \mathbf{G}_d \begin{bmatrix} F_u \\ F_v \end{bmatrix} \tag{5.3}$$

With:

$$\mathbf{G}_d(1,1) = \mathbf{G}_d(2,2) = \frac{\frac{1}{k}\left(\frac{s^2}{{\omega_0}^2} + 2\xi\frac{s}{\omega_0} + 1 - \frac{\Omega^2}{{\omega_0}^2}\right)}{\left(\frac{s^2}{{\omega_0}^2} + 2\xi\frac{s}{\omega_0} + 1 - \frac{\Omega^2}{{\omega_0}^2}\right)^2 + \left(2\frac{\Omega}{\omega_0}\frac{s}{\omega_0}\right)^2} \tag{5.4a}$$

$$\mathbf{G}_d(1,2) = -\mathbf{G}_d(2,1) = \frac{\frac{1}{k}\left(2\frac{\Omega}{\omega_0}\frac{s}{\omega_0}\right)}{\left(\frac{s^2}{{\omega_0}^2} + 2\xi\frac{s}{\omega_0} + 1 - \frac{\Omega^2}{{\omega_0}^2}\right)^2 + \left(2\frac{\Omega}{\omega_0}\frac{s}{\omega_0}\right)^2} \tag{5.4b}$$

Neglecting the damping for simplicity ($\xi \ll 1$), the direct terms have two complex conjugate zeros:

$$z = \pm j\sqrt{\omega_0^2 - \omega^2} \tag{5.5}$$

Which are between the two pairs of complex conjugate poles at:

$$p_1 = \pm j(\omega_0 - \omega) \tag{5.6}$$

$$p_2 = \pm j(\omega_0 + \omega) \tag{5.7}$$

Therefore, for $\Omega < \sqrt{k/m}$ (i.e. stable system), the transfer functions for Relative Damping Control have **alternating complex conjugate poles and zeros**.

5.2 Decentralized Relative Damping Control

The transfer functions from $[F_u,\ F_v]$ to $[d_u,\ d_v]$ is identified and shown in Figure 5.2 for several rotating velocities.

In order to see if large damping can be added with Relative Damping Control, the root locus is computed (Figure 5.3). The closed-loop system is unconditionally stable and the poles can be damped as much as wanted.

5.3 Damped Plant

Let's select a reasonable "Relative Damping Control" gain, and compute the closed-loop damped system. The open-loop and damped plants are compared in Figure 5.4.

The rotating aspect does not add any complexity for the use of Relative Damping Control. It does not increase the low frequency coupling as compared to Integral Force Feedback.

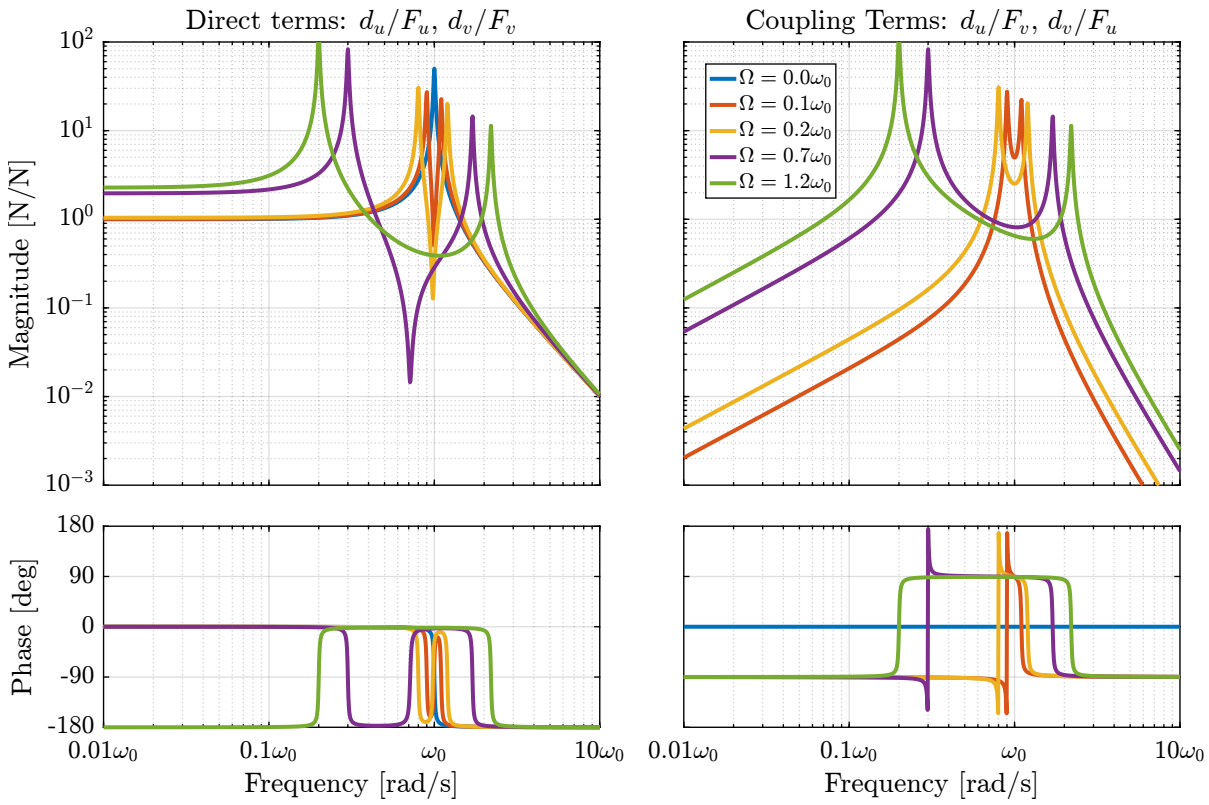

Figure 5.2: Bode plot of the direct and coupling term for the "relative damping control" plant - Effect of rotation

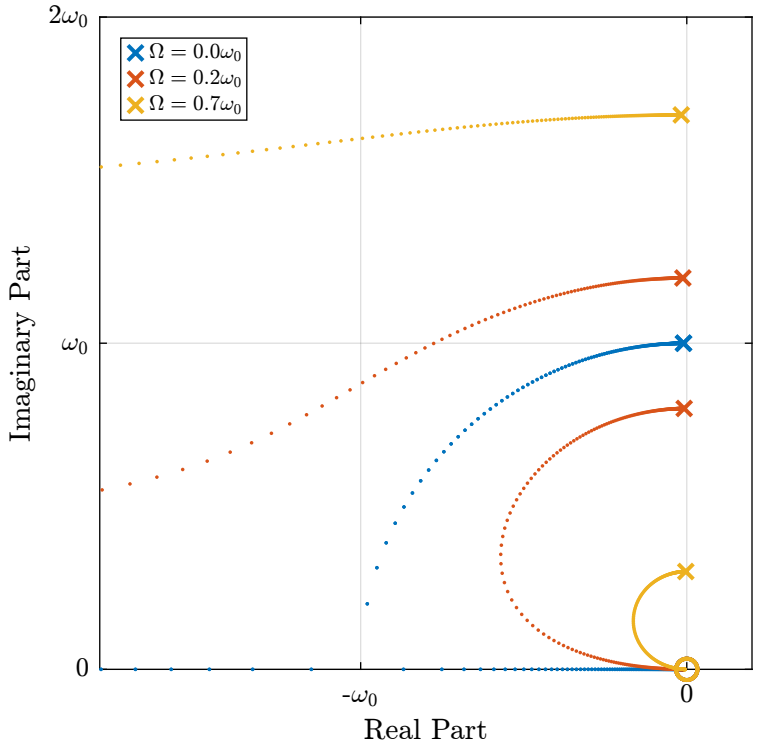

Figure 5.3: Root Locus for Relative Damping Control

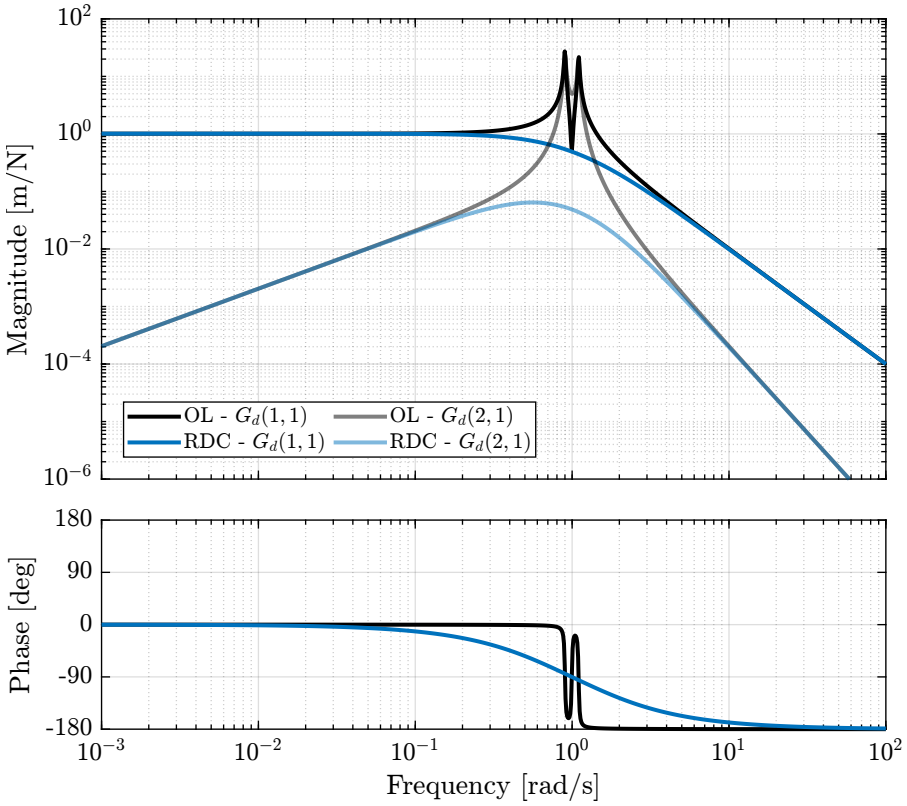

Figure 5.4: Damped plant using Relative Damping Control

6 Comparison of Active Damping Techniques

These two proposed IFF modifications as well as relative damping control are now compared in terms of added damping and closed-loop behavior.

For the following comparisons, the cut-off frequency for the added HPF is set to $\omega_i = 0.1\omega_0$ and the stiffness of the parallel springs is set to $k_p = 5m\Omega^2$ (corresponding to $\alpha = 0.05$). These values are chosen based on previous discussion about optimal parameters.

6.1 Root Locus

Figure 6.1 shows the Root Locus plots for the two proposed IFF modifications as well as for relative damping control. While the two pairs of complex conjugate open-loop poles are identical for both IFF modifications, the transmission zeros are not. This means that the closed-loop behavior of both systems will differ when large control gains are used.

One can observe that the closed loop poles corresponding to the system with added springs (in red) are bounded to the left half plane implying unconditional stability. This is not the case for the system where the controller is augmented with an HPF (in blue).

It is interesting to note that the maximum added damping is very similar for both techniques.

6.2 Obtained Damped Plant

The actively damped plants are computed for the three techniques and compared in Figure 6.2.

Important

It is shown that while the diagonal (direct) terms of the damped plants are similar for the three active damping techniques, of off-diagonal (coupling) terms are not. Integral Force Feedback strategy is adding some coupling at low frequency which may negatively impact the positioning performances.

6.3 Transmissibility And Compliance

The proposed active damping techniques are now compared in terms of closed-loop transmissibility and compliance.

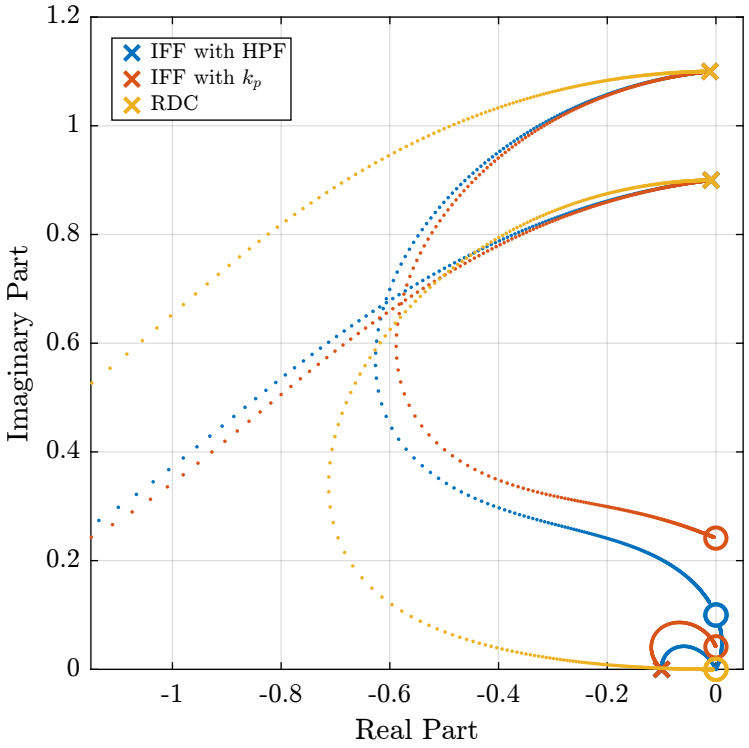

Figure 6.1: Comparison of active damping techniques for rotating platform - Root Locus

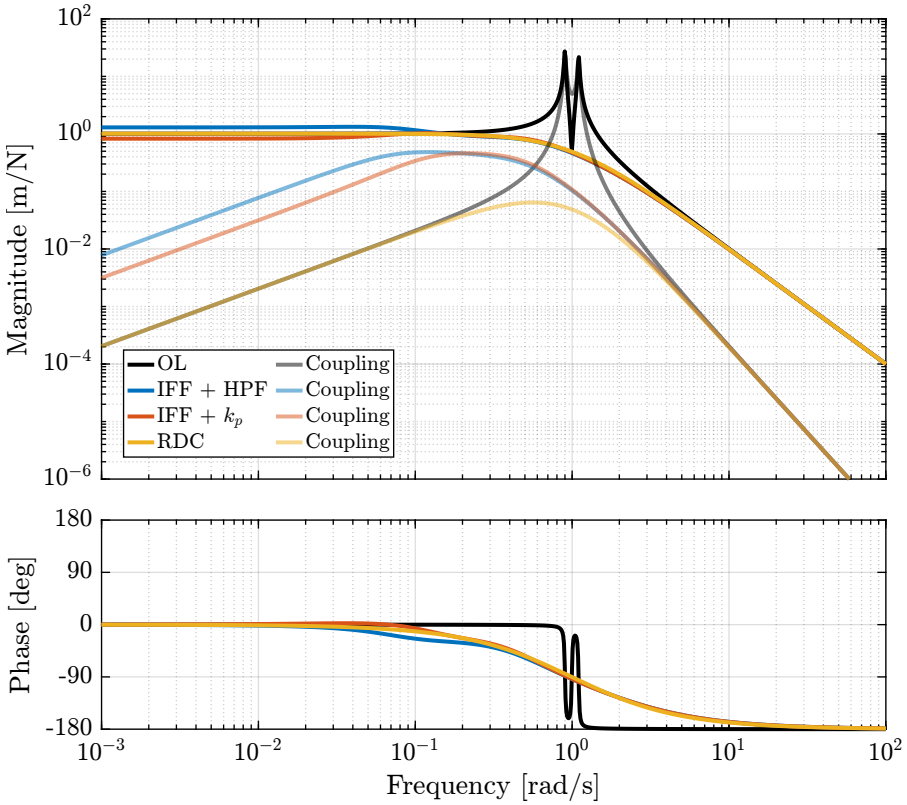

Figure 6.2: Comparison of the damped plants obtained with the three active damping techniques

The transmissibility is here defined as the transfer function from a displacement of the rotating stage along $\vec{i}_x$ to the displacement of the payload along the same direction. It is used to characterize how much vibration is transmitted through the suspended platform to the payload.

The compliance describes the displacement response of the payload to external forces applied to it. This is a useful metric when disturbances are directly applied to the payload. It is here defined as the transfer function from external forces applied on the payload along $\vec{i}_x$ to the displacement of the payload along the same direction.

Very similar results are obtained for the two proposed IFF modifications in terms of transmissibility and compliance (Figure 6.3).

Important

Using IFF degrades the compliance at low frequency while using relative damping control degrades the transmissibility at high frequency. This is very well known characteristics of these common active damping techniques that holds when applied to rotating platforms.

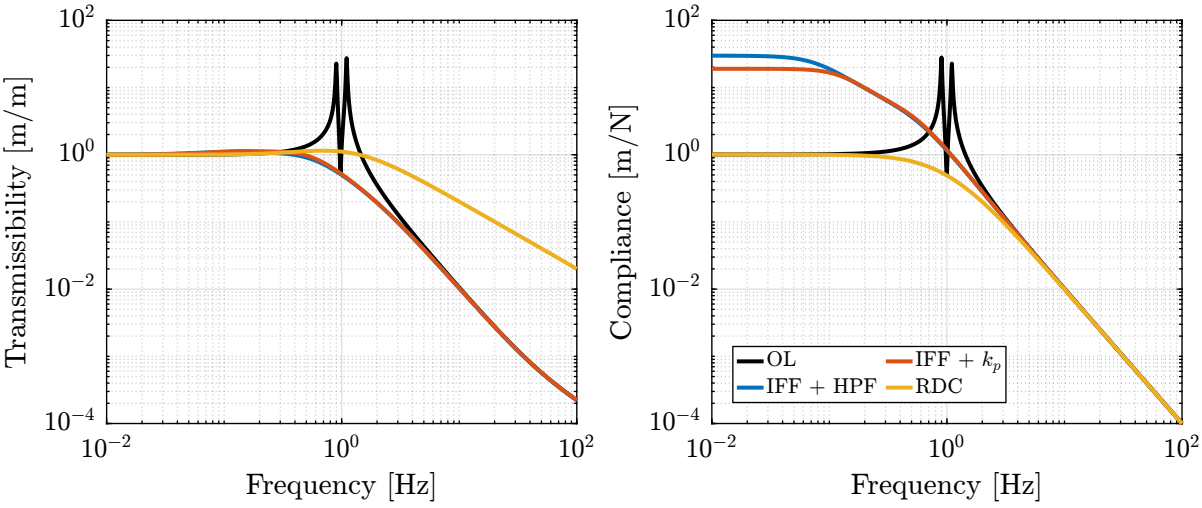

Figure 6.3: Comparison of the obtained transmissibilty and compliance for the three tested active damping techniques

7 Rotating Nano-Hexapod

The current analysis is now applied on a model representing the rotating nano-hexapod.

Three nano-hexapod stiffnesses are tested: $k_n = 0.01\,\text{N}/\mu\text{m}$, $k_n = 1\,\text{N}/\mu\text{m}$ and $k_n = 100\,\text{N}/\mu\text{m}$.

Only the maximum rotating velocity is considered ($\Omega = 60\,\text{rpm}$) with the light sample ($m_s = 1\,\text{kg}$) as this is the worst identified case scenario.

7.1 Nano-Active-Stabilization-System - Plant Dynamics

For the NASS, the maximum rotating velocity is $\Omega = 2\pi\,\text{rad}\,\text{s}^{-1}$ for a suspended mass on top of the nano-hexapod's actuators equal to $m_n + m_s = 16\,\text{kg}$. The parallel stiffness corresponding to the centrifugal forces is $m\Omega^2 \approx 0.6\,\text{N}\,\text{mm}^{-1}$.

The transfer functions from nano-hexapod actuator force F_u to the displacement of the nano-hexapod in the same direction d_u as well as in the orthogonal direction d_v (coupling) are shown in Figure 7.1 for all three considered nano-hexapod stiffnesses.

Important

It is shown that the rotation has the largest effect on the soft nano-hexapod:

- larger coupling (the ratio of the coupling term to the direct term is larger for the sort nano-hexapod)
- larger shift of poles as a function of the rotating velocity

7.2 Optimal IFF with High Pass Filter

Let's apply Integral Force Feedback with an added High Pass Filter to the three nano-hexapods.

First, let's find the parameters of the IFF controller that yield best simultaneous damping. The results are shown in Figure 7.2. The added damping for the soft nano-hexapod is quite low and is limited by the maximum usable gain.

The IFF parameters are chosen as follow:

- for $k_n = 0.01\,\text{N}/\mu\text{m}$: ω_i is chosen such that the maximum damping is achieved while the gain is less than half of the maximum gain at which the system is unstable. This is done to have some control robustness.

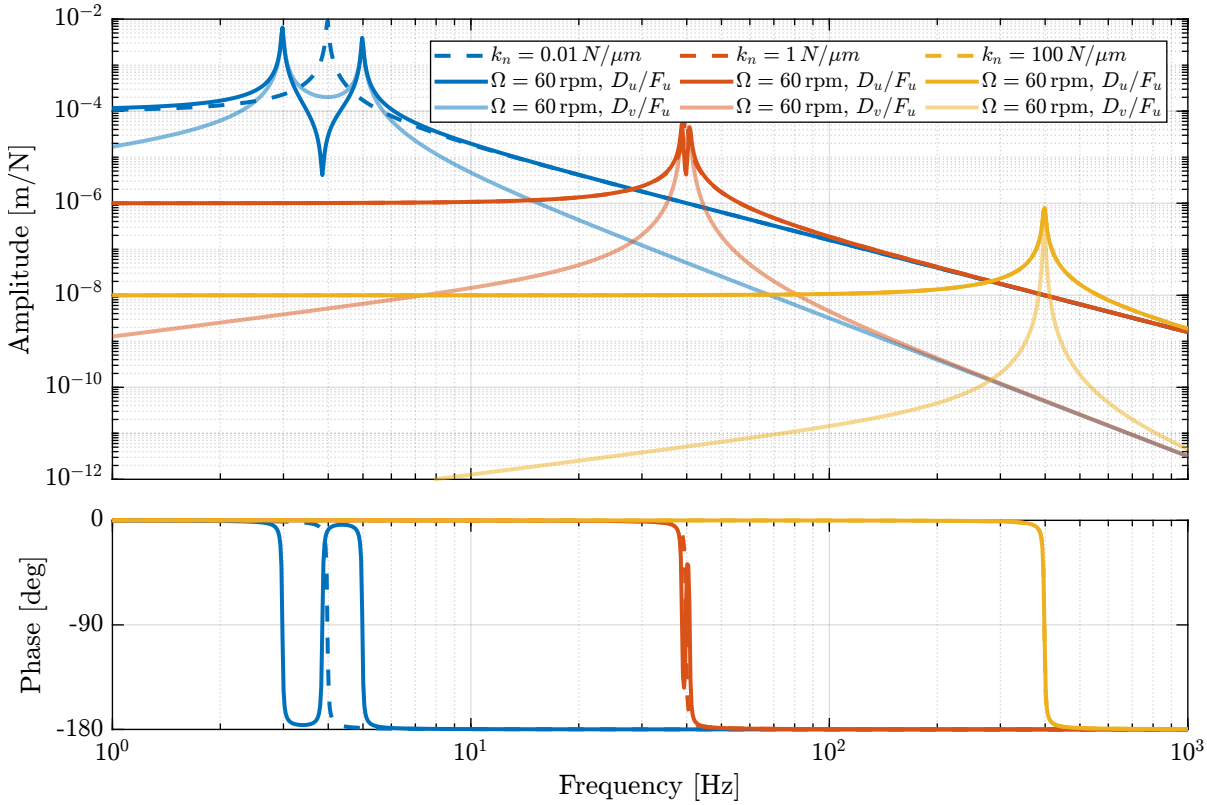

Figure 7.1: Effect of rotation on the nano-hexapod dynamics - Dashed lines are the plants without rotation, solid lines are plants at maximum rotating velocity, and shaded lines are coupling terms at maximum rotating velocity

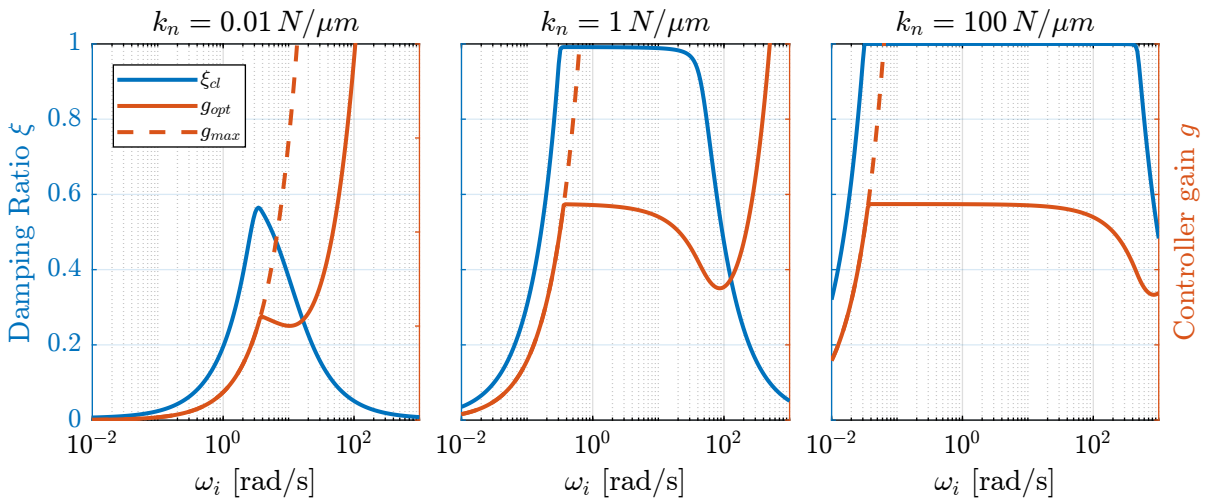

Figure 7.2: Optimal high pass filter cut-off frequency ω_i that yields maximum simultaneous damping

- for $k_n = 1\,\mathrm{N}/\mu\mathrm{m}$ and $k_n = 100\,\mathrm{N}/\mu\mathrm{m}$: the largest ω_i is chosen such that obtained damping is 95 % of the maximum achievable damping. Large ω_i is chosen here to limit the loss of compliance and the increase of coupling at low frequency as was shown in Section 3.

The obtained IFF parameters and the achievable damping are summarized in Table 7.1.

Table 7.1: Obtained optimal parameters for the modified IFF controller

	ω_i	g	ξ
$k_n = 0.01\,N/\mu m$	7.32	51.13	0.45
$k_n = 1\,N/\mu m$	39.17	426.95	0.93
$k_n = 100\,N/\mu m$	499.45	3774.63	0.94

The Root Locus for all three nano-hexapods are shown in Figure 7.3 with included optimal chosen gains.

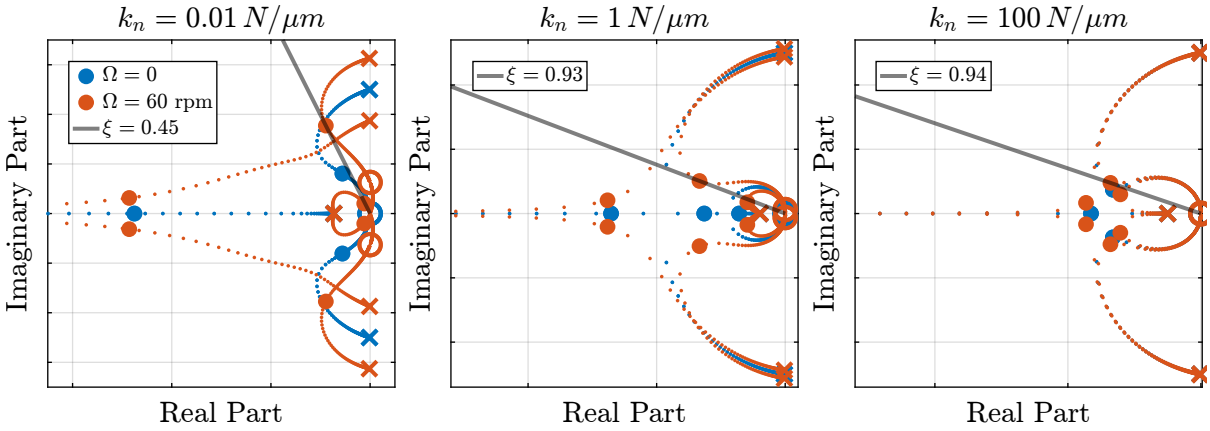

Figure 7.3: Root Locus for modified IFF with high pass filter. Optimal ω_i is used. The three nano-hexapod stiffnesses are compared. The grey line indicates the minimum damping obtained with the optimal chosen control parameters.

7.3 Optimal IFF with Parallel Stiffness

For each considered nano-hexapod stiffness, the parallel stiffness k_p is varied from $k_{p,\min} = m\Omega^2$ (the minimum stiffness to have unconditional stability) to $k_{p,\max} = k_n$ (the total nano-hexapod stiffness). In order to keep the overall stiffness constant, the actuator stiffness k_a is decreased when k_p is increased:

$$k_a = k_n - k_p \tag{7.1}$$

With k_n the total nano-hexapod stiffness.

An high pass filter is also added to limit the low frequency gain. The cut-off frequency ω_i is chosen to be one tenth of the system resonance:

$$\omega_i = \omega_0/10 \tag{7.2}$$

The achievable maximum simultaneous damping of all the modes is computed as a function of the parallel stiffnesses. The comparison for the nano-hexapod stiffnesses is done in Figure 7.4. It is shown

that **the soft nano-hexapod cannot yield good damping**. For the two stiff options, the achievable damping starts to significantly decrease when the parallel stiffness is one tenth of the total stiffness $k_p = k_n/10$.

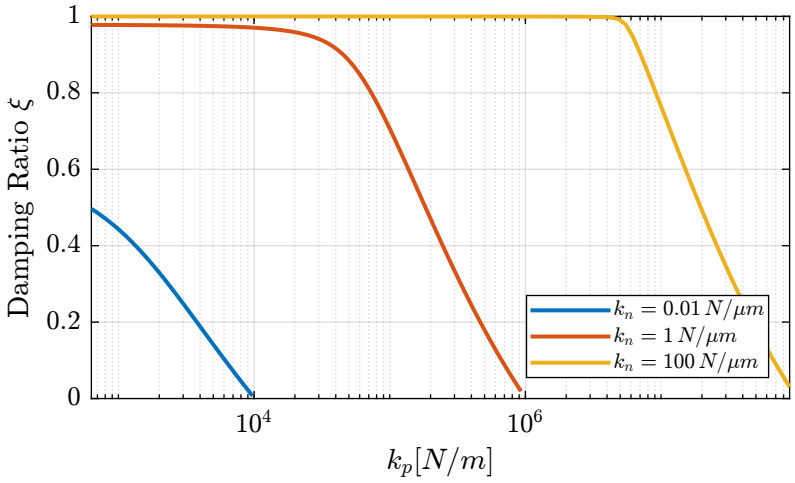

Figure 7.4: Maximum achievable simultaneous damping with IFF as a function of the parallel stiffness for all three nano-hexapod stiffnesses

Let's choose $k_p = 10^3\,\mathrm{N\,m^{-1}}$, $k_p = 10^4\,\mathrm{N\,m^{-1}}$ and $k_p = 10^6\,\mathrm{N\,m^{-1}}$ for the three considered nano-hexapods respectively based on Figure 7.4.

The corresponding optimal controller gains are shown in Table 7.2.

Table 7.2: Obtained optimal parameters for the modified IFF controller

	g	ξ_{opt}
$k_n = 0.01\,N/\mu m$	47.9	0.44
$k_n = 1\,N/\mu m$	465.57	0.97
$k_n = 100\,N/\mu m$	4624.25	1.0

The root locus for the three nano-hexapod with parallel stiffnesses are shown in Figure 7.5.

Important

Similarly to what was found with the IFF and added High Pass Filter:

- the stiff nano-hexapod is less affected by the rotation than the soft one
- the achievable damping is much larger with the stiff nano-hexapods

7.4 Optimal Relative Motion Control

For each considered nano-hexapod stiffness, relative damping control is applied and the achievable damping ratio as a function of the controller gain is shown in Figure 7.6.

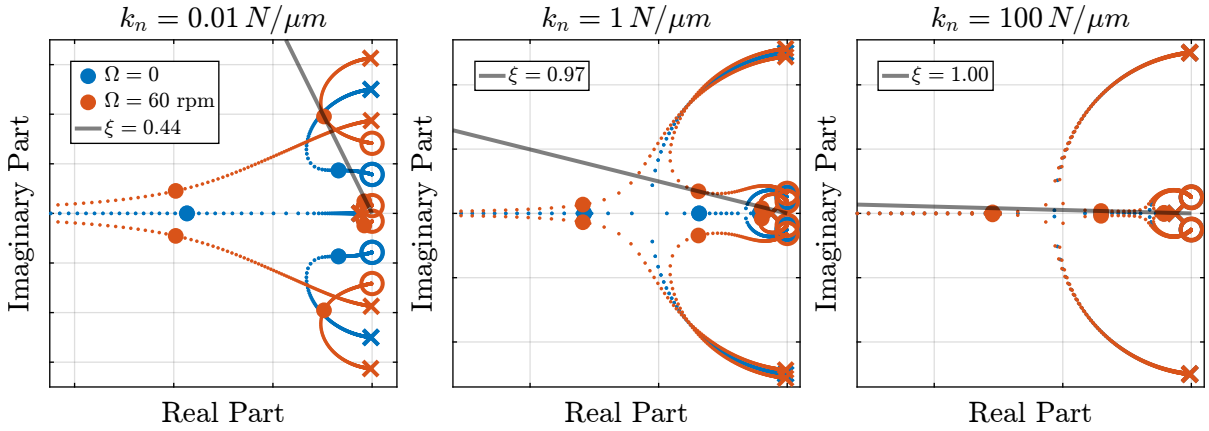

Figure 7.5: Root Locus for optimal parameters (IFF + k_p strategy) - Comparison of attainable damping with the three nano-hexapod stiffnesses

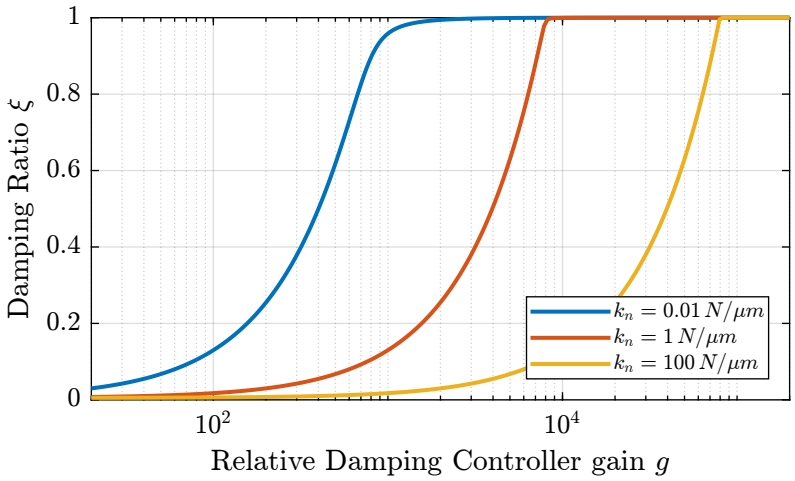

Figure 7.6: Achievable simultaneous damping with "Relative Damping Control" as a function of the controller gain for all three nano-hexapod stiffnesses

The gain is chosen is chosen such that 99% of modal damping is obtained. The root locus for all three nano-hexapod stiffnesses are shown in Figure 7.7.

Important

Relative damping control is much less impacted by gyroscopic effects. It can be easily applied on the nano-hexapod with and without rotation without much differences.

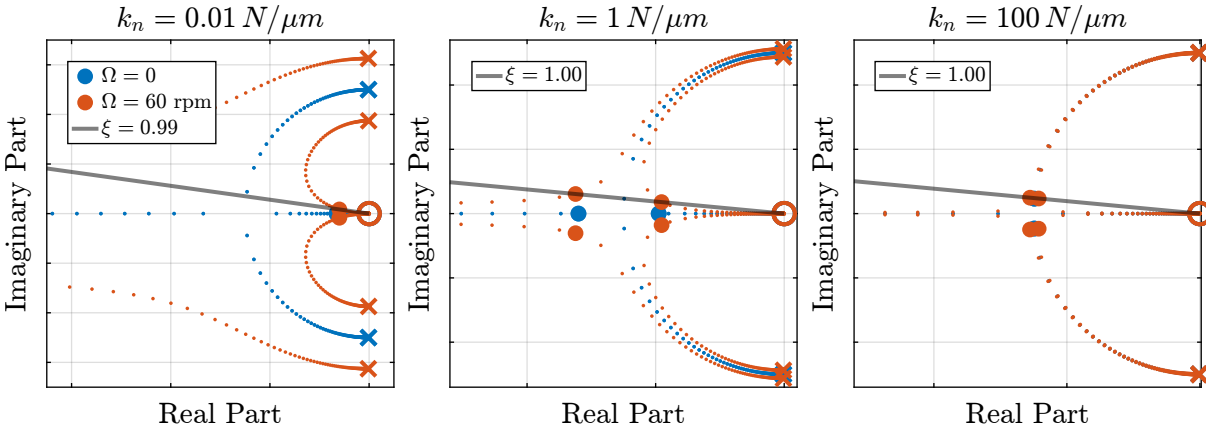

Figure 7.7: Root Locus for optimal parameters - Comparison of attainable damping with the soft and moderately stiff nano-hexapods

7.5 Comparison of the obtained damped plants

Let's now compare the obtained damped plants for the three active damping techniques applied on the three nano-hexapod stiffnesses (Figure 7.8).

Important

Similarly to what was concluded in previous analysis:

- IFF adds coupling below the resonance frequency as compared to the open-loop and RDC cases
- Add three methods are yielding good damping, except for IFF applied on the soft nano-hexapod where things are more complicated
- Coupling is smaller for stiff nano-hexapods

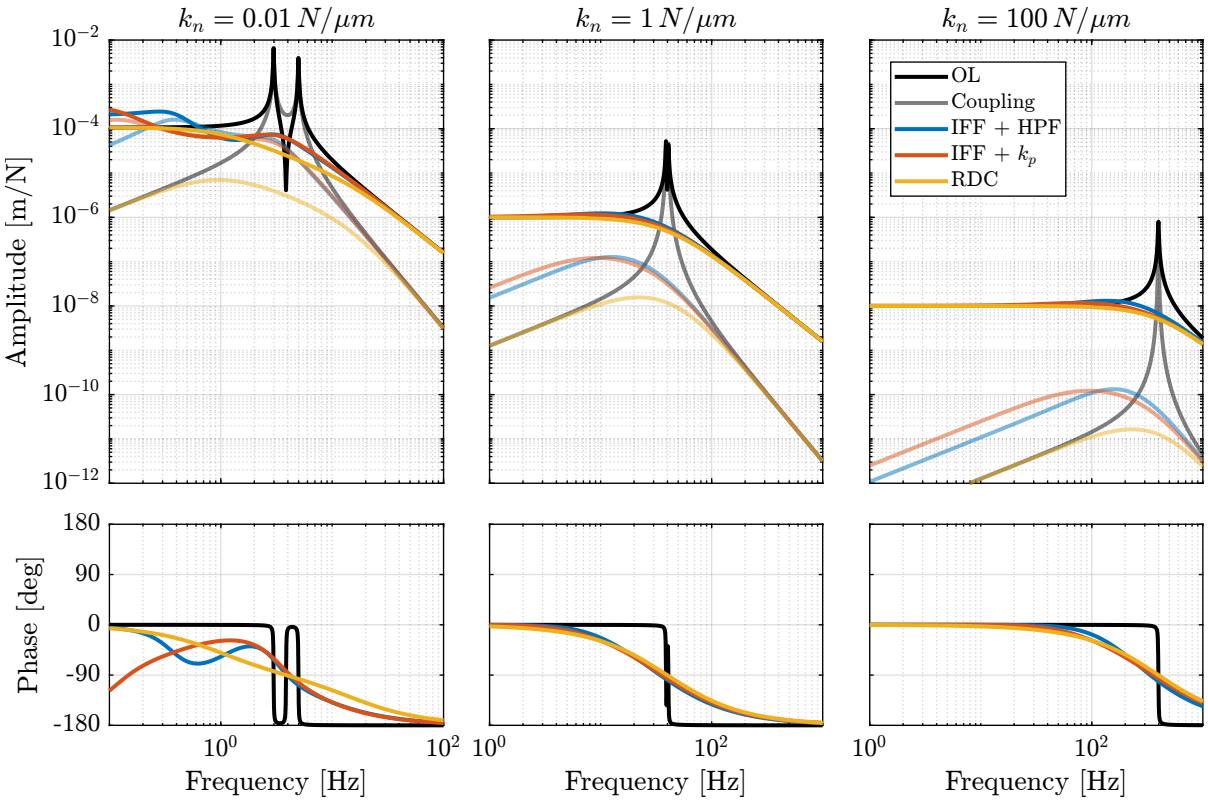

Figure 7.8: Comparison of the damped plants (direct and coupling terms) for the three proposed active damping techniques (IFF with HPF, IFF with k_p and RDC) applied on the three nano-hexapod stiffnesses. $\Omega = 60\,\text{rmp}$ and $m_n + m_s = 16\,\text{kg}$.

8 Nano-Active-Stabilization-System with rotation

Up until now, the model used consisted of an infinitely stiff vertical rotating stage with a X-Y suspended stage.

While quite simplistic, this allowed to study the effects of rotation and the associated limitations when active damping is to be applied.

In this section, the limited compliance of the micro-station is taken into account as well as the rotation of the spindle.

8.1 NASS model

In order to be a bit closer to the NASS application, the 2DoF nano-hexapod (modelled as shown in Figure 1.1) is now located on top of a model of the micro-station including (see Figure 8.1 for a 3D view):

- the floor whose motion is imposed
- a 2DoF granite ($k_{g,x} = k_{g,y} = 950\,\text{N}/\mu\text{m}$, $m_g = 2500\,\text{kg}$)
- a 2DoF T_y stage ($k_{t,x} = k_{t,y} = 520\,\text{N}/\mu\text{m}$, $m_g = 600\,\text{kg}$)
- a spindle (vertical rotation) stage whose rotation is imposed ($m_s = 600\,\text{kg}$)
- a 2DoF micro-hexapod ($k_{h,x} = k_{h,y} = 61\,\text{N}/\mu\text{m}$, $m_g = 15\,\text{kg}$)

A payload is rigidly fixed to the nano-hexapod and the x, y motion of the payload is measured with respect to the granite.

8.2 System dynamics

The dynamics of the undamped and damped plants are identified. The active damping parameters used are the optimal ones previously identified (i.e. for the rotating nano-hexapod fixed on a rigid platform).

The undamped and damped plants are shown in Figure 8.2. Three nano-hexapod velocities are shown (from left to right): $k_n = 0.01\,\text{N}/\mu\text{m}$, $k_n = 1\,\text{N}/\mu\text{m}$ and $k_n = 100\,\text{N}/\mu\text{m}$. The direct terms are shown

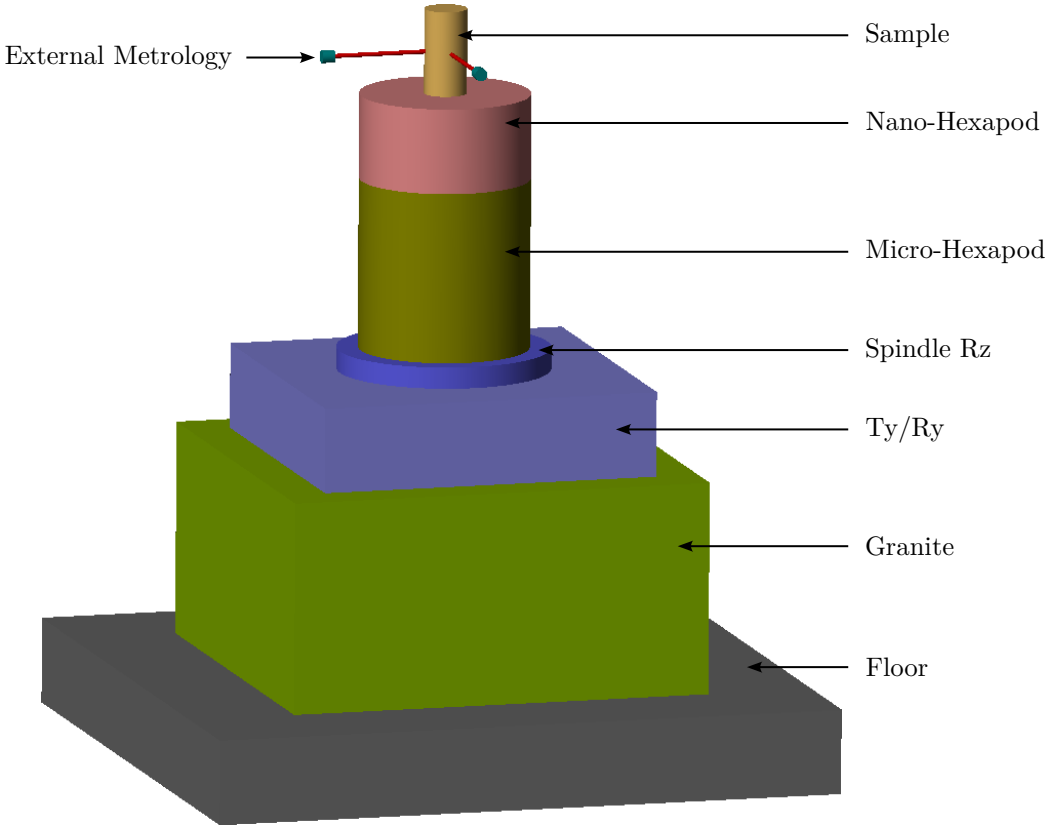

Figure 8.1: 3D view of the Nano-Active-Stabilization-System model.

by the solid curves while the coupling terms are shown by the shaded ones.

Important

It can be observed on Figure 8.2 that:

- Coupling (ratio between the off-diagonal and direct terms) is larger for the soft nano-hexapod
- Damping added by the three proposed techniques is quite high and the obtained plant is rather easy to control
- There is some coupling between nano-hexapod and micro-station dynamics for the stiff nano-hexapod (mode at 200Hz)
- The two proposed IFF modification yields similar results

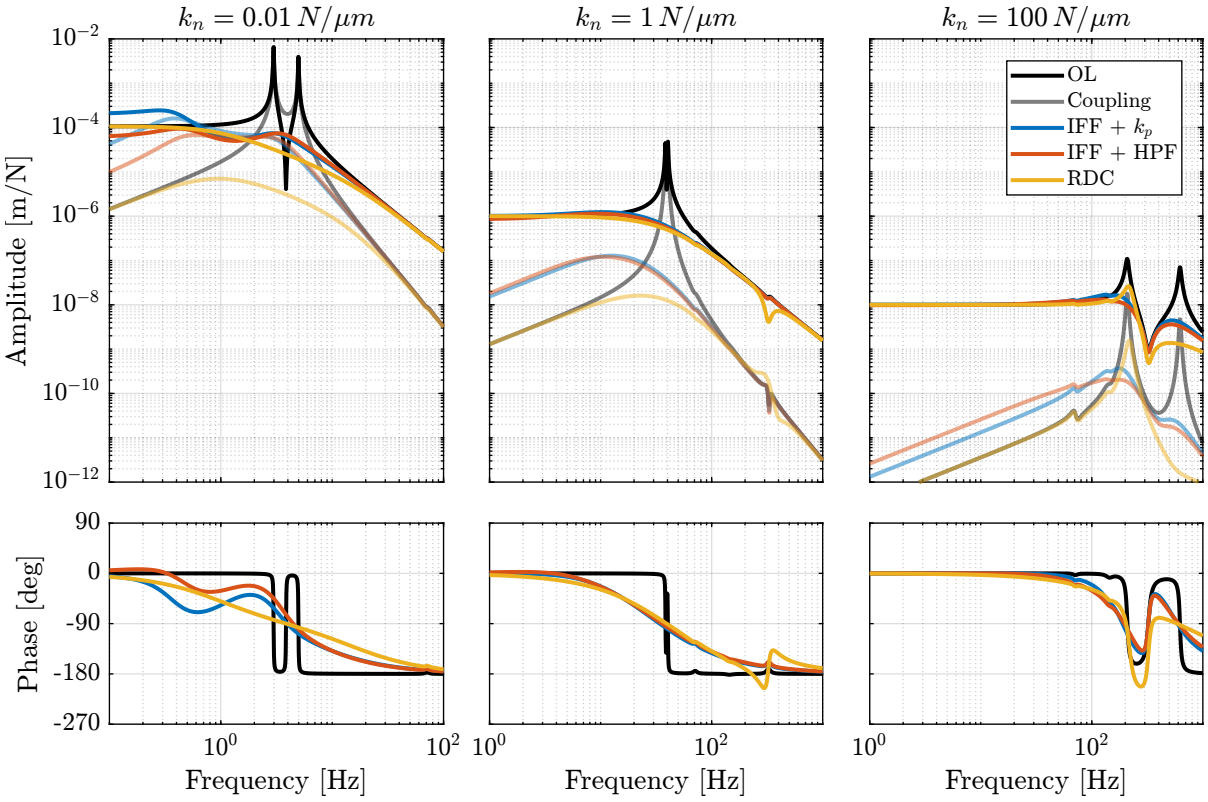

Figure 8.2: Bode plot of the transfer function from nano-hexapod actuator to measured motion by the external metrology

To confirm that the coupling is smaller when the stiffness of the nano-hexapod is increase, the *coupling ratio* for the three nano-hexapod stiffnesses are shown in Figure 8.3.

8.3 Effect of disturbances

The effect of three disturbances are considered:

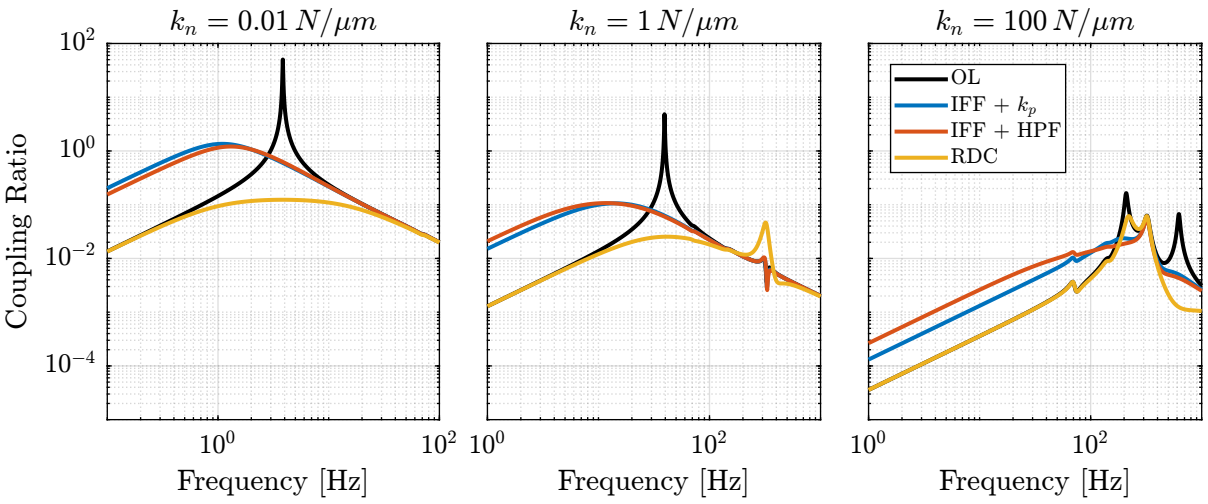

Figure 8.3: Coupling ratio for the proposed active damping techniques evaluated for the three nano-hexapod stiffnesses

- Floor motion (Figure 8.4)
- Micro-Station vibrations (Figure 8.5)
- Direct force applied on the payload (Figure 8.6)

Important

Conclusions are similar than with the uniaxial (non-rotating) model:

- Regarding the effect of floor motion and forces applied on the payload:
  - The stiffer, the better (magnitudes are lower for the right curves, Figures 8.4 and 8.6)
  - Integral Force Feedback degrades the performances at low frequency compared to relative damping control
- Regarding the effect of micro-station vibrations:
  - Having a soft nano-hexapod allows to filter these vibrations between the suspensions modes of the nano-hexapod and some flexible modes of the micro-station. Using relative damping control reduce this filtering (Figure 8.5, left).

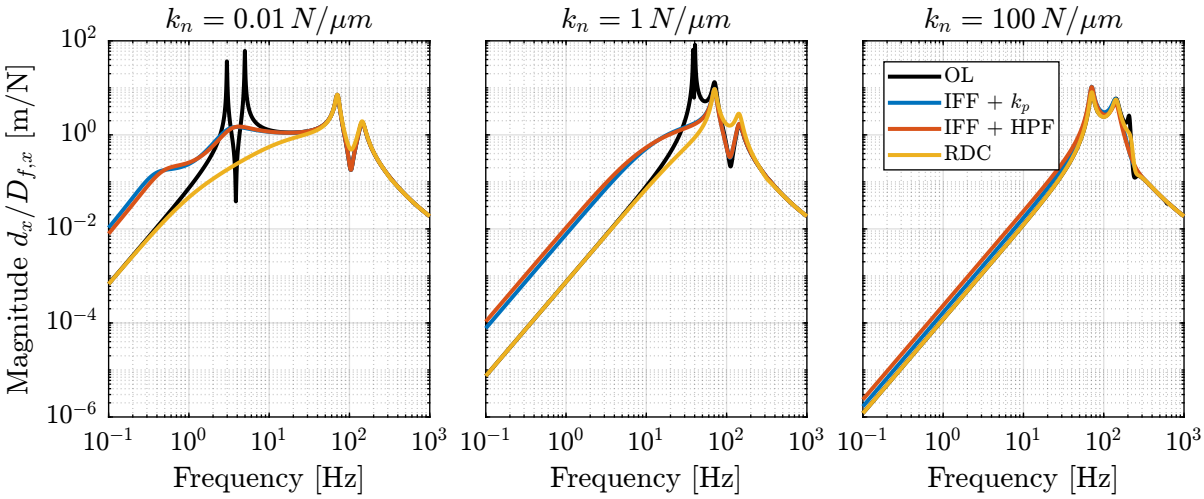

Figure 8.4: Effect of Floor motion on the position error - Comparison of active damping techniques for the three nano-hexapod stiffnesses

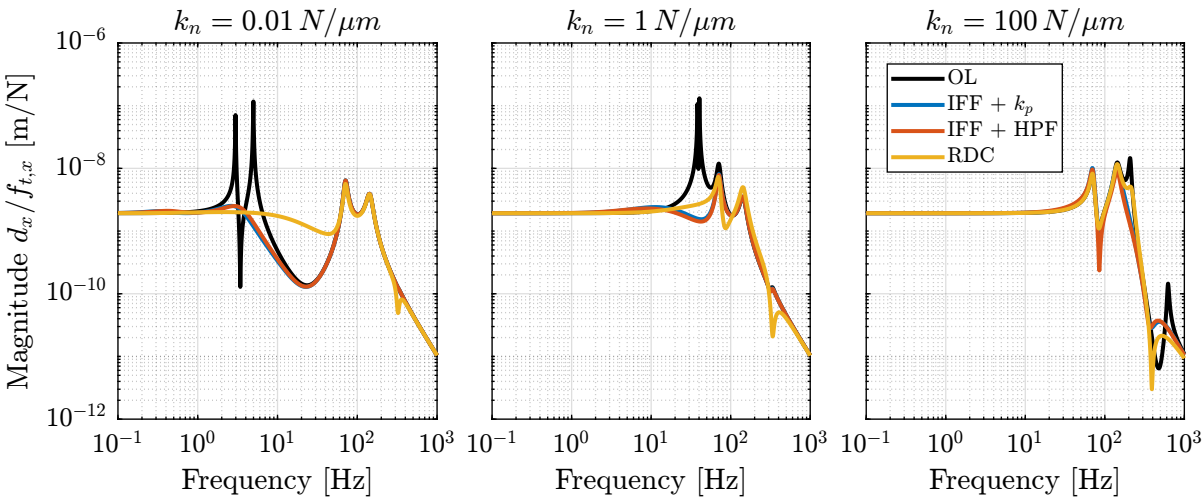

Figure 8.5: Effect of micro-station vibrations on the position error - Comparison of active damping techniques for the three nano-hexapod stiffnesses

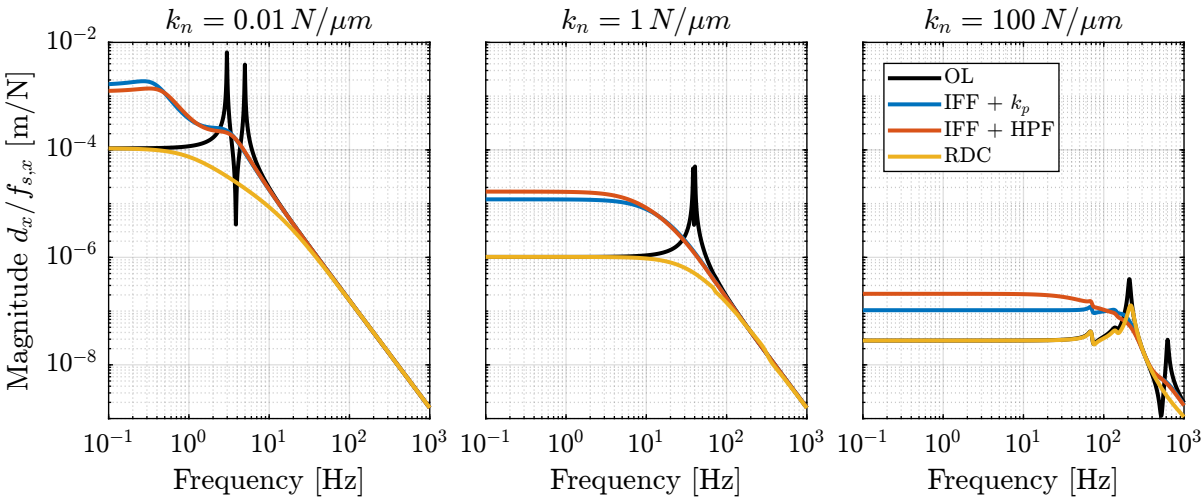

Figure 8.6: Effect of sample forces on the position error - Comparison of active damping techniques for the three nano-hexapod stiffnesses

9 Conclusion

In this study, the gyroscopic effects induced by the spindle's rotation have been studied using a spindle model (Section 1). Decentralized IFF with pure integrators was shown to be unstable when applied to rotating platforms (Section 2). Two modifications of the classical IFF control have been proposed to overcome this issue.

The first modification concerns the controller and consists of adding an high pass filter to the pure integrators. This is equivalent as to moving the controller pole to the left along the real axis. This allows the closed loop system to be stable up to some value of the controller gain (Section 3).

The second proposed modification concerns the mechanical system. Additional springs are added in parallel with the actuators and force sensors. It was shown that if the stiffness k_p of the additional springs is larger than the negative stiffness $m\Omega^2$ induced by centrifugal forces, the classical decentralized IFF regains its unconditional stability property (Section 4).

These two modifications were compared with relative damping control in Section 6. While having very different implementations, both proposed modifications were found to be very similar when it comes to the attainable damping and the obtained closed loop system behavior.

Then, this study has been applied to a rotating system that corresponds to the nano-hexapod parameters (Section 7). To be closer to the real system dynamics, the limited compliance of the micro-station has been taken into account. Results show that the two proposed IFF modifications can be applied for the NASS even in the presence of spindle rotation.

Bibliography

[1] C. Collette, S. Janssens, and K. Artoos, "Review of active vibration isolation strategies," *Recent Patents on Mechanical Engineeringe*, vol. 4, no. 3, pp. 212–219, 2011 (cit. on p. 10).

[2] H. Lin and J. E. McInroy, "Disturbance attenuation in precise hexapod pointing using positive force feedback," *Control Engineering Practice*, vol. 14, no. 11, pp. 1377–1386, 2006 (cit. on p. 10).

[3] J. Fanson and T. K. Caughey, "Positive position feedback control for large space structures," *AIAA journal*, vol. 28, no. 4, pp. 717–724, 1990 (cit. on p. 10).

[4] A. Preumont, J.-P. Dufour, and C. Malekian, "Active damping by a local force feedback with piezoelectric actuators," in *32nd Structures, Structural Dynamics, and Materials Conference*, American Institute of Aeronautics and Astronautics, Apr. 1991 (cit. on pp. 10, 14, 15).

[5] D. Karnopp, M. J. Crosby, and R. Harwood, "Vibration control using semi-active force generators," *Journal of Engineering for Industry*, 1974 (cit. on p. 10).

[6] M. Serrand and S. Elliott, "Multichannel feedback control for the isolation of base-excited vibration," *Journal of Sound and Vibration*, vol. 234, no. 4, pp. 681–704, 2000 (cit. on p. 10).

[7] A. Preumont, A. François, F. Bossens, and A. Abu-Hanieh, "Force feedback versus acceleration feedback in active vibration isolation," *Journal of Sound and Vibration*, vol. 257, no. 4, pp. 605–613, 2002 (cit. on p. 10).

[8] A. Preumont, J.-P. Dufour, and C. Malekian, "Active damping by a local force feedback with piezoelectric actuators," *Journal of guidance, control, and dynamics*, vol. 15, no. 2, pp. 390–395, 1992 (cit. on p. 10).

[9] A. Preumont, B. De Marneffe, and S. Krenk, "Transmission zeros in structural control with collocated multi-input/multi-output pairs," *Journal of guidance, control, and dynamics*, vol. 31, no. 2, pp. 428–432, 2008 (cit. on pp. 10, 14).

[10] Y. R. Teo and A. J. Fleming, "Optimal integral force feedback for active vibration control," *Journal of Sound and Vibration*, vol. 356, pp. 20–33, Nov. 2015 (cit. on p. 10).

[11] S. Chesné, A. Milhomem, and C. Collette, "Enhanced damping of flexible structures using force feedback," *Journal of Guidance, Control, and Dynamics*, vol. 39, no. 7, pp. 1654–1658, 2016 (cit. on p. 10).

[12] G. Zhao, A. Paknejad, A. Deraemaeker, and C. Collette, "$\mathcal{H}_\infty$ Optimization of an integral force feedback controller," *Journal of Vibration and Control*, vol. 25, no. 17, pp. 2330–2339, 2019 (cit. on p. 10).

[13] S. Skogestad and I. Postlethwaite, *Multivariable Feedback Control: Analysis and Design*. John Wiley, 2007 (cit. on p. 14).

[14] B. de Marneffe, "Active and passive vibration isolation and damping via shunted transducers," Ph.D. dissertation, Université Libre de Bruxelles, Brussels, Belgium, 2007 (cit. on p. 15).

[15] A. Preumont, *Vibration Control of Active Structures - Fourth Edition* (Solid Mechanics and Its Applications). Springer International Publishing, 2018 (cit. on p. 23).